

ENGINEERING

Aspiration-assisted bioprinting for precise positioning of biologics

Bugra Ayan^{1,2,*}, Dong Nyoung Heo^{1,2,3*}, Zhifeng Zhang¹, Madhuri Dey^{2,4}, Adomas Povilianskas¹, Corina Drapaca¹, Ibrahim T. Ozbolat^{1,2,5,6†}

Three-dimensional (3D) bioprinting is an appealing approach for building tissues; however, bioprinting of mini-tissue blocks (i.e., spheroids) with precise control on their positioning in 3D space has been a major obstacle. Here, we unveil “aspiration-assisted bioprinting (AAB),” which enables picking and bioprinting biologics in 3D through harnessing the power of aspiration forces, and when coupled with microvalve bioprinting, it facilitated different biofabrication schemes including scaffold-based or scaffold-free bioprinting at an unprecedented placement precision, ~11% with respect to the spheroid size. We studied the underlying physical mechanism of AAB to understand interactions between aspirated viscoelastic spheroids and physical governing forces during aspiration and bioprinting. We bioprinted a wide range of biologics with dimensions in an order-of-magnitude range including tissue spheroids (80 to 600 μm), tissue strands (~800 μm), or single cells (electrocytes, ~400 μm), and as applications, we illustrated the patterning of angiogenic sprouting spheroids and self-assembly of osteogenic spheroids.

INTRODUCTION

Aggregated cells have been formed into spheroids (1–3), honeycombs (4), and strands (5) from a variety of different cell types and their cocultures. They have many advantages including the cellular capability to secrete extracellular matrix (ECM) components with an effective communication between cells in a native-like microenvironment (1). When cells are grown in an isolated fashion (i.e., cells in monolayers or cell-laden hydrogels), they usually do not facilitate native-like tissue microenvironment because of limited cell-cell and cell-ECM interactions (6). Three-dimensional (3D) cell aggregates, particularly tissue spheroids, are excellent candidates to mimic in vivo tissue microenvironments, which can be reconstituted to form reproducible complex tissues [such as bone (7) and pancreas (8)] and or tissue models [cancer (9)]. Furthermore, cocultured aggregates can be used as building blocks for fabricating scalable tissue complexes (2). Spheroids loaded with endothelial cells can also facilitate a denser tissue microenvironment, inherent ECM secretion, and prevascularized network (10). As a result, large-scale vascularized tissue complexes can be biofabricated using prevascularized cell aggregates as fundamental building blocks (7, 11), which allow more accurate representations of native tissues. Moreover, these tissue complexes stand to develop physiologically correct models for drug screening, disease modeling (i.e., cancer), and high-throughput screening (12). Therefore, various advantages of tissue spheroids make them a great candidate as building blocks for 3D bioprinting.

Despite these advantages, only a few methods including extrusion-based bioprinting (2, 11, 13, 14), droplet-based bioprinting (15), Kengan (16), and biogripper approaches (4, 17) have been demon-

strated for 3D bioprinting of spheroids made of cells, such as but not limited to human articular or nasal chondrocytes, human umbilical vein endothelial cells (HUVECs), human umbilical vein smooth muscle cells, etc. Extrusion-based bioprinting technique dispenses similar-sized spheroids suspended in a hydrogel ink through a glass nozzle. During bioprinting, spheroids in the hydrogel ink may self-aggregate inside the nozzle, leading to clogging issues (2). Although extrusion-based bioprinting of cellular aggregates in the form of strands can generate scalable tissues (3, 5), their use in high-precision applications, such as organ-on-a-chip platforms or microphysiological systems, is quite challenging. In droplet-based bioprinting, a single spheroid is loaded into a droplet during bioprinting, which enables the positioning of spheroids in 2D (15). Kengan method uses an array of needles on which spheroids are skewered by a robotic arm; however, this method requires same-size spheroids since bioprinted spheroids have to fit properly in the needle array and smaller spheroids would be prone to fragment during insertion on the needle (16). Recently, the biogripper technique was introduced to manipulate defined micro-molded tissue blocks. However, this technique enables bioprinting of only molded tissue blocks in the range of 600 μm to 3.4 mm, where submillimeter scale is quite large for typical tissue building blocks (4, 17). All the existing techniques used in the literature suffer from the positional accuracy and precision of spheroid bioprinting; may induce substantial damage to biological, structural, and mechanical properties of spheroids; and are limited to the use of same-size spheroids for successful bioprinting.

Here, we present a new hybrid bioprinting approach through harnessing the power of aspiration forces, which enables us to pick and precisely bioprint a wide of range of biologics, with dimensions in an order-of-magnitude range (80 to 800 μm), into/onto a gel substrate with minimal cellular damage. To better understand the response of biologics to the bioprinting process, we unveil the underlying mechanism explaining the physical behavior of viscoelastic spheroids and their interactions with physical governing forces during aspiration, lifting, and bioprinting. Compared to the abovementioned methods, the presented approach facilitated the bioprinting of spheroids in higher positional precision and accuracy, ~11 and

Copyright © 2020
The Authors, some
rights reserved;
exclusive licensee
American Association
for the Advancement
of Science. No claim to
original U.S. Government
Works. Distributed
under a Creative
Commons Attribution
NonCommercial
License 4.0 (CC BY-NC).

¹Engineering Science and Mechanics Department, Penn State University, University Park, PA 16802, USA. ²The Huck Institutes of the Life Sciences, Penn State University, University Park, PA 16802, USA. ³Department of Dental Materials, School of Dentistry, Kyung Hee University, Seoul 02447, Republic of Korea. ⁴Department of Chemistry, Penn State University, University Park, PA 16802, USA. ⁵Biomedical Engineering Department, Penn State University, University Park, PA 16802, USA. ⁶Materials Research Institute, Penn State University, University Park, PA 16802, USA.

*These authors contributed equally to this work.

†Corresponding author. Email: ito1@psu.edu

~15% with respect to the spheroid size, respectively. In addition, it enabled bioprinting in 3D with flexibility of bioprinting of nonuniform, any-size spheroids into (i) a functional gel as a scaffold-based approach or (ii) a sacrificial gel as a scaffold-free approach (Fig. 1). The newly developed aspiration-assisted bioprinting (AAB) platform, modified from a MakerBot Replicator 1 (<\$1000) (see fig. S1), operates a custom-made glass pipette, which is used to “pick up” biologics and “3D bioprint” them into or onto a gel substrate. AAB was coupled with microvalves for droplet-based bioprinting of functional or sacrificial hydrogels. To bioprint spheroids into a functional hydrogel (i.e., fibrin), fibrinogen and thrombin layers were printed via microvalve bioprinting to obtain fibrin constructs. Spheroids were then bioprinted into desired positions before the constructs were fully cross-linked. To bioprint spheroids onto a sacrificial hydrogel (i.e., alginate), microvalve bioprinting and aerosol cross-linking processes were used. The first step included the generation of sodium alginate droplets on a glass substrate. Second, calcium chloride (CaCl_2) was fumed for instant cross-linking (18). Spheroids were then picked and 3D bioprinted onto the partially cross-linked alginate. Next, the print area was overlaid with sodium alginate droplets. Then, aerosol form of CaCl_2 was applied again. The process was then repeated as many times as needed for building other layers. Next, bioprinted spheroids were maintained in the support gel temporally until partial fusion was realized. Last, the support gel was gently removed through decross-linking using a lyase solution.

The presented approach paves the way for bioprinting several tissue types and a wide range of spheroids in 2D and 3D in gel substrates with multiple applications presented throughout this paper, including (i) the development of physiologically relevant culture environments to demonstrate the collective angiogenic sprouting behavior of spheroids in a scaffold medium and (ii) fabrication of osteogenic tissues to decode the role of midterm osteogenic induction of stem cell-based spheroids (before bioprinting) on the mineralization and assembly behavior in a scaffold-free environment. In addition to spheroids, other living cells and tissue building blocks, including electrocytes from electric eel and tissue strands, can be bioprinted for a wide variety of applications, such as but not limited to tissue engineering, regenerative medicine, drug testing and pharmaceuticals, disease modeling, microphysiological systems, biophysics, and biocomputing.

RESULTS AND DISCUSSION

Working mechanism of AAB

In the AAB process, the first step is to pick a spheroid (fig. S2) and then lift it and drag it rapidly outside the culture media by aspiration forces as shown in Fig. 2A. The spheroid should be captured with a minimum aspiration force to transfer but not break or damage it. During aspiration under an applied stress (σ), a spheroid with viscoelastic properties exhibits both viscous and elastic properties (19). It exhibits elastic properties like a solid at times shorter than

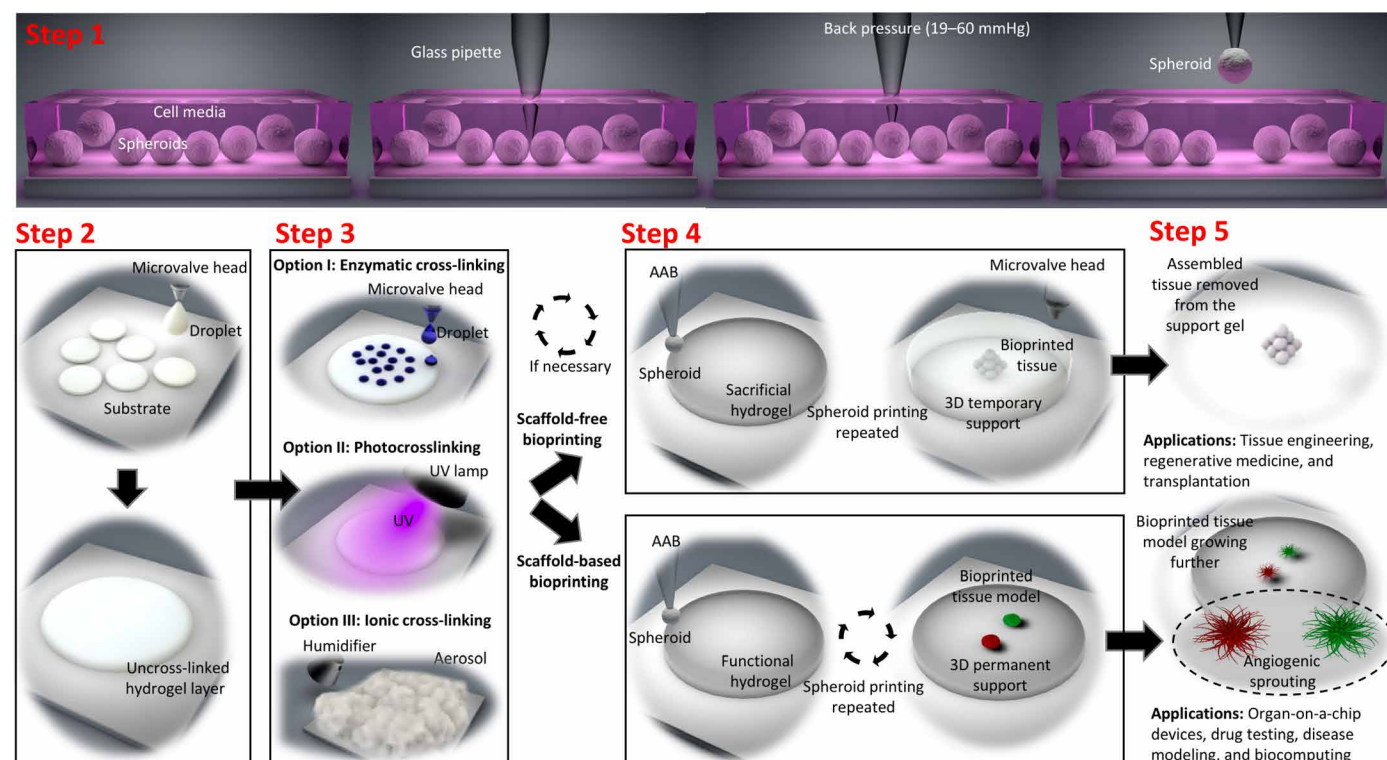


Fig. 1. Step-by-step illustration of picking and bioprinting of spheroids. In step 1, spheroids are picked from the cell media by a glass pipette, where required back pressure is set to lift spheroids. Afterward, spheroids can be bioprinted into sacrificial hydrogels (scaffold-free bioprinting) or functional hydrogels (scaffold-based bioprinting). In this regard, in step 2, microvalve bioprinting is used to bioprint a gel substrate, which can then be partially cross-linked using various different cross-linking schemes—such as but not limited to enzymatic, photo, and ionic cross-linking—as highlighted in step 3. Next, in step 4, spheroids are bioprinted precisely into designed positions, and spheroid bioprinting is repeated as many times as needed. Steps 2 to 4 can be repeated as needed. In step 5, bioprinted tissues are isolated from the support hydrogel (for scaffold-free bioprinting) or further grown in the functional hydrogel (for scaffold-based bioprinting). UV, ultraviolet.

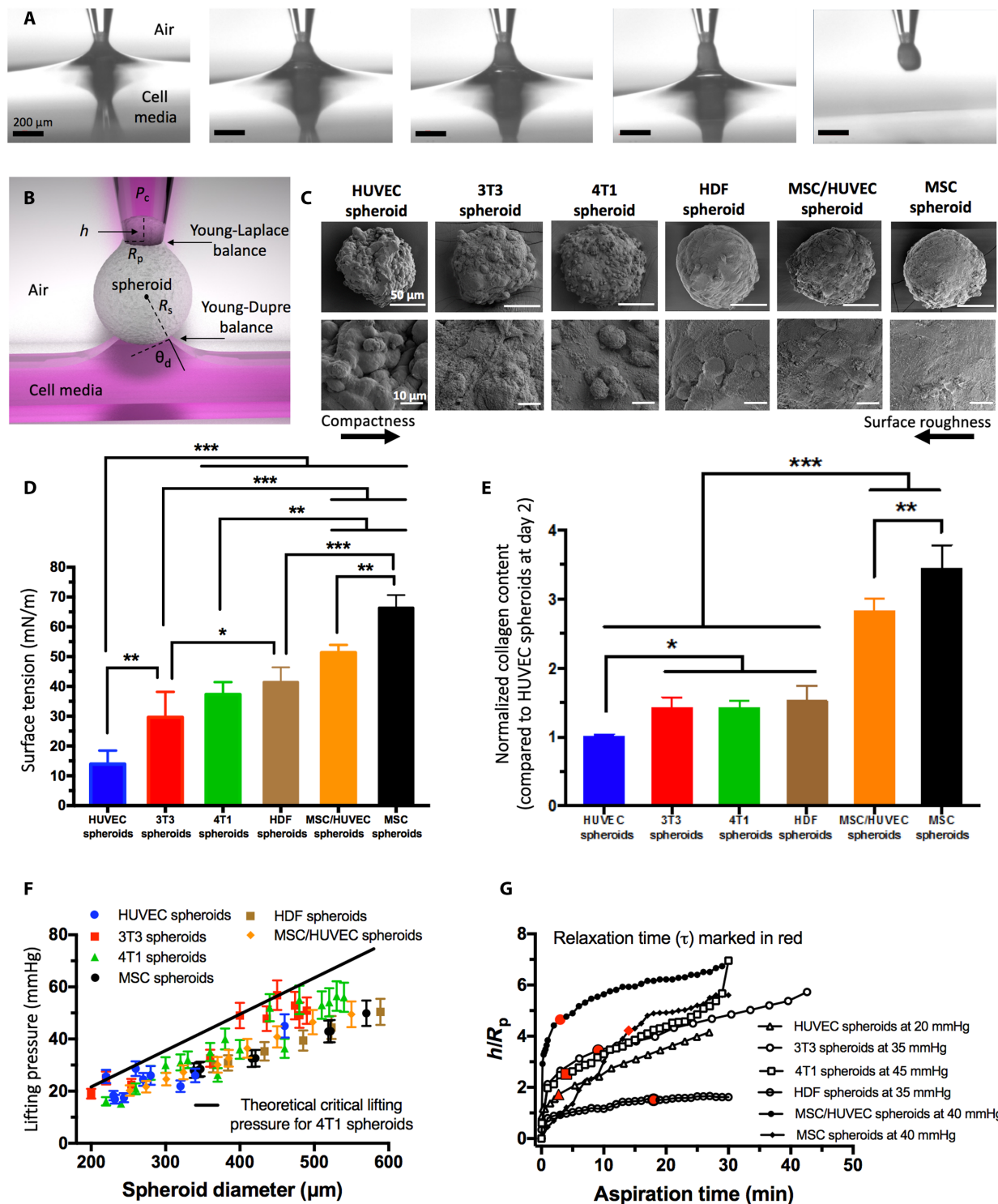


Fig. 2. Picking and lifting spheroids. (A) Time-lapse images during spheroid lifting process (at the interface of cell media and air). (B) A schematic showing physical parameters involved in lifting of a spheroid from the cell media. (C) SEM images, (D) surface tension ($n = 5$), and (E) the normalized collagen content of HUVEC, 3T3, 4T1, HDF, MSC/HUVEC, and MSC spheroids (compared to HUVEC spheroids) at day 2 ($n = 4$; $*P < 0.05$, $**P < 0.01$, and $***P < 0.001$). (F) Critical lifting pressure to lift spheroids (in the range of 200 to 600 μm in diameter) ($n = 5$). The experimental data spread under the theoretical curve, which was determined using the experimental data for 4T1 spheroids with parameters ($\theta_d = 64^\circ$ and $\sigma_{1,2} = 57.4$ mN/m). Spheroids made of other cell types had lower theoretical critical lifting pressure values (data are not shown in the paper). For instance, the theoretical critical lifting pressure for HUVEC spheroids was 20% smaller than that of 4T1 spheroids. (G) Viscoelastic behavior of spheroids under aspiration ($n = 3$). Here, h denotes the advancement of spheroids inside a glass pipette. The aspiration experiment used a similar pipette as that in bioprinting. The aspiration pressure was determined according to the size of spheroids satisfying the condition that spheroids could be lifted from the cell media.

relaxation time τ and like a fluid for $t > \tau$, which can be described by the Maxwell model

$$\frac{d\sigma}{dt} + \frac{\sigma}{\tau} = \lambda \frac{d\epsilon}{dt} \quad (1)$$

where ϵ is the strain and λ is the modulus of elasticity of spheroids. During this process, two major impediments were experienced. First, spheroids were prone to fragment because of low cellular cohesivity and elasticity even under very low pressure levels. Second, detachment of spheroids from the pipette tip at the three-phase contact (air-liquid-tissue) was observed during lifting. The former can be mitigated by engineering of spheroids to attain better elastic properties [such as culturing them longer (20) or incorporating cells expressing higher cell-cell and cell-matrix adhesion or ECM proteins (21)], and the latter can be addressed by determining the minimum aspiration pressure (critical lifting pressure). A spheroid is lifted by pipette aspiration after overcoming gravity, buoyance force, hydraulic drag, and thermodynamic barrier at the interface. The main difficulty in lifting a spheroid is the binding energy caused by the surface tension at the interface between the culture media and air. The spheroid contributes to the lifting barrier in the form of a contact angle at the three-phase (tissue, air, and media) contact line. The energy barrier to lift a spheroid into air can be expressed as

$$E = A_s \sigma_{1,2} \cos^2 \frac{\theta_d}{2} \quad (2)$$

where A_s is the surface area of a spheroid, $\sigma_{1,2}$ is the surface tension between the media and air, and θ_d is the contact angle at the three-phase contact line. During lifting, the three-phase contact angle (dynamic contact angle) is greater than the static contact angle because of dynamics effect (22). The dynamic contact angles of spheroids made of several types of cells were enumerated in table S1. By comparison, the thermodynamics barrier is about 500 times of gravity, 100 times of Stokes' drag, and 5 times of Young-Dupre critical pressure. During lifting, the energy barrier can be estimated by adding a geometrical correction factor (m) as a result of slight changes in the spheroid geometry due to the aspiration of a tongue (see Fig. 2B). The initial contact length of the tongue ($h_{t=0}$) of a spheroid ranges between R_p and $2R_p$. Thus, m can be defined as follows

$$m = 1 - \frac{4\pi R_p^2}{4\pi R_s^2 - 4\pi R_p^2} = 1 - \frac{R_p^2}{R_s^2 - R_p^2} \approx 1 - \left(\frac{R_p}{R_s}\right)^2 \quad (3)$$

In Eq. 3, R_p is the pipette tip radius and R_s is the spheroid radius. m can be approximated to 1 when the spheroid radius is much larger than the radius of the pipette tip. However, when lifting a small spheroid or when the radius of the pipette is comparable to that of the spheroid, m becomes much smaller. Consequently, the critical lifting pressure of a spheroid (P_C) from the media can be expressed as follows (22)

$$P_C = mF_{max}/A_h = 2mR_s\sigma_{1,2}\cos^2\frac{\theta_d}{2}/(\pi R_p^2) \quad (4)$$

The critical lifting pressure is proportional to the surface tension coefficient of the media-air interface, the radius of the spheroid, the dynamic contact angle at the three-phase contact line, and the tapered angle of the pipette (influences R_p , but this parameter was fixed).

To demonstrate picking and lifting of spheroids, we fabricated a wide range of spheroid types with different viscoelastic and surface tension properties using HUVECs, mouse fibroblast cell line (3T3), mouse mammary carcinoma line (4T1), human dermal fibroblasts (HDFs), coculture of human mesenchymal stem cells (MSCs) and HUVECs, and MSCs. Various kinds of spheroids in a diameter range of 200 to 600 μm were obtained using cell-repellent 96-well plates. Spheroids were fabricated at a cell density from 2500 to 10,000 per spheroid and cultured for 1 to 3 days (fig. S3A). During the first 24 hours, we closely monitored spheroid formation and observed that 3T3 and HDF spheroids became compact and withstood aspiration forces at the end of 20 hours, while others became compact at 24 hours, implying that these spheroids could be lifted anytime thereafter (fig. S4). To investigate the ultrastructure of spheroids, spheroids were analyzed by scanning electron microscopy (SEM), and SEM images demonstrated clear differences in surface morphology and compactness of different spheroids cultured for 2 days (Fig. 2C). The surface topology of MSC spheroids displayed a substantial amount of secreted ECM with smoother and more compact structure due to tight cell-cell and cell-ECM interactions. On the other hand, the surface topology of HUVEC spheroids displayed lesser ECM compound, which resulted in a pitted surface and tiny gaps between cells. To lift spheroids, spheroids were required to be compact and captured in the cell media and to withstand aspiration forces. Spheroids also have surface tension, with each cell being analogous to a liquid molecule (23, 24). Thus, surface tension of spheroids were investigated by a micropipette aspiration technique (19, 25) according to the Young-Laplace equation, which gave the relationship between the internal pressure of spheroids and cell media across a curved interface. According to the Young-Laplace equation, the surface tension coefficient can be estimated as $\sigma = \frac{\Delta P}{2(1/R_p - 1/R_s)}$, where ΔP is the equilibrium aspiration pressure when the advancement of the spheroid inside the pipette was the same as the radius of the pipette tip. As shown in Fig. 2D, the surface tension of HUVEC, 3T3, 4T1, HDF, MSC/HUVEC, and MSC spheroids at 2 days of culture were measured to be ~14, 30, 37, 41, 51, and 66 mN/m, respectively. Surface tension of MSC-only spheroids was approximately five times higher than that of HUVEC spheroids. It is worth mentioning that Norotte *et al.* (26) used a different method to measure the surface tension of spheroids and obtained a similar result for HUVEC spheroids. While the surface tension of 4T1, HDF, and MSC/HUVEC spheroids increased over time, the surface tension of spheroids made from other cell types maintained similar properties during the 3-day culture (fig. S3B). This time frame, on the other hand, can vary for spheroids prepared using other techniques, such as but not limited to hanging drop, microfluidic, rotator flask, and liquid overlay methods (27). Our results indicate that there is a positive correlation between the surface tension of spheroids and their compactness, confirming previous findings by Foty and Steinberg (28). In addition, the total collagen amount of spheroids was investigated using a hydroxyproline colorimetric assay kit since collagen is one of the major ECM components of spheroids (3). The measured collagen amount for 3T3, 4T1, HDF, MSC/HUVEC, and MSC spheroids at day 2 was ~1.4-, 1.4-, 1.5-, 2.8-, and 3.4-fold higher compared to that for HUVEC spheroids, respectively (Fig. 2E). The normalized collagen content in different spheroids showed a similar trend as compared to the compactness of spheroids; however, we did not observe any notable differences among the normalized collagen content for 3T3, 4T1, and HDF spheroids. A recent study

reported a positive correlation between compactness of cell aggregates and their collagen expression (29).

Figure 2F denotes a linear relationship between the critical lifting pressure and diameter of spheroids (in the range of 200 to 600 μm). When the diameter of spheroids increased, the critical lifting pressure also increased. The theoretical critical lifting pressure for each spheroid types at different diameters were determined using Eq. 4, where the maximum theoretical value belonged to 4T1 spheroids, which could be used as a baseline for other spheroid types to be tested during aspiration. In addition, the minimum critical lifting pressure among all spheroids types (from 200 to 600 μm) was determined to be ~ 19 mmHg. The difference between the theoretical and experimental value of the critical lifting pressure was due to (i) the irregular shape of spheroids (elliptic or pancake-like) influencing the maximum energy barrier (30, 31) and (ii) the measurement inaccuracy of the pressure sensor (which was around 10%; see fig. S5, A and B). Another vital factor for successful bioprinting was to determine viscoelastic properties of spheroids, which were reflected by the relationship between stress and strain as a function of time. During the AAB process, spheroids were kept within a solid elastic regime. The operation time of AAB was defined by the elapsed time between spheroid picking and bioprinting, which was commonly less than 30 s. Therefore, spheroids were successfully bioprinted, while their relaxation time (τ) was longer than the bioprinting operation time. For this reason, we plotted the aspiration curves of various spheroids (Fig. 2G). At the early stage of aspiration, spheroids deformed very quickly within the elastic regime. Then, after a relaxation time, accumulated stress was gradually released, and spheroids experienced a “relaxation” process and return to their original shapes. As shown in Fig. 2G, the relaxation time for HUVEC, 4T1, and MSC/HUVEC spheroids were around 3 to 5 min. The relaxation time for HDF spheroids could reach up to 18 min. Overall, these relaxation times were sufficient to assure successful bioprinting without permanent deformation to spheroids.

After lifting spheroids from the cell media and transferring them to the bioprinting stage, the back pressure was released, and the spheroids were fully recovered or, in other words, they returned to their original shapes as bioprinting time was less than the relaxation time. To bioprint a spheroid, the spheroid was partially submerged into a precross-linked or partially cross-linked gel substrate, as going deeper could result in their breakage due to penetration of the pipette tip into the spheroid. When the nozzle moved up, the spheroid was stuck to the gel because of adherence between the spheroid and the gel (Fig. 3A1), released from the pipette, and deposited into the gel. In AAB, successful bioprinting was determined by a constant adherence at the pipette tip (upward, F_{up}) and a variable bioprinting force at the interface of gel (downward, F_{down}). To determine F_{up} , two angles were defined: $\beta_1 = \arccos \frac{R_p}{R_s}$, and β_2 is the pipette taper angle. F_{up} can be expressed as $F_{\text{up}} = 2\pi R_p \gamma_s \cos(\beta_1 + \beta_2)$, where γ_s is the surface tension of the spheroid. At the bottom of the spheroid, the maximum force pulling the spheroid downward due to the surface tension of the gel substrate, i.e., the maximum bioprinting force provided by the gel, can be expressed as $F_{\text{down}} = 2\pi R_s \gamma_g \cos^2\left(\frac{\theta_1}{2}\right)$. Here, γ_g is the surface tension of the gel, and θ_1 is the effective angle of wetting. For successful bioprinting, the maximum force pulling the spheroid downward needs to overcome the surface tension adherence at the tip of the pipette. Thus, successful printing, as shown in Fig. 3A2, needs to satisfy the condition $F_{\text{down}} > F_{\text{up}}$. However, if a spheroid is not fully recovered (when the spheroid is submerged

rapidly into the gel), there can be an extra stress (F_{ext}) at the pipette tip. The extra stress may increase the difficulty of bioprinting since F_{down} needs to overcome $F_{\text{ext}} + F_{\text{up}}$.

To verify the presented theoretical approach, we measured β_1 , β_2 , and θ_1 angles and obtained the surface tension of precross-linked gel [1% (w/v) alginate] from the literature (32). The results indicated that F_{down} was ~ 32 , 14, 12, 11, 9, and 7 times greater than F_{up} for HUVEC, 3T3, 4T1, HDF, MSC/HUVEC, and MSC spheroids, respectively, as enumerated in table S2. Surface tension of gel solutions can vary from gel to gel. In some gels [such as alginate (32)], surface tension is dependent on concentration; however, there are hydrogels where surface tension is not dependent on concentration, such as polyacrylamide (33). Therefore, we cannot make a general statement on the correlation between concentration and surface tension. In addition, concentration of the gel should also be compatible with microvalve bioprinting, as higher concentrations of precursor solutions are, in general, bioprintable as such concentrations can support droplet formation (34). For bioprinting into a gel substrate, the gel precursor solution should be flowable as well so that the solution can overlay the bioprinted spheroid quickly; therefore, we performed bioprinting on partially cross-linked or uncross-linked gel precursor.

Capabilities of AAB in patterning and 3D bioprinting of biologics

Before performing the patterning and 3D bioprinting of spheroids, we first inspected the quality of positioning during bioprinting. In this regard, agarose beads (with near-perfect sphericity) and the motion stage of the 3D bioprinter were used as control groups. The positional precision and accuracy for the motion stage (empty pipettes), spherical agarose beads (ranging from 250 to 300 μm in diameter), and 2-day cultured MSC/HUVEC spheroids (~ 300 μm in diameter) were determined to be ~ 2 and 2.1 μm , 14.4 and 10.4 μm , and 34.7 and 45.9 μm , respectively (fig. S5, C to E). The results indicate that the bioprinter motion stage had a small effect on the positional error during bioprinting and that bioprinting of spheroids was about two- and fourfold less precise and accurate compared to printing of agarose beads, respectively. This could be due to the viscoelastic nature, lesser sphericity, and slightly higher average diameter of tissue spheroids compared to more rigid agarose beads. We demonstrated the ability to bioprint spheroids precisely ($\sim 11\%$ with respect to the average spheroid size) onto alginate through patterning of various shapes (fig. S6, A1 to A3), initials of Penn State University (PSU) (Fig. 3A3), and a matrix of spheroids of various shapes and dimensions (including irregular shapes) in the diameter range of 80 to 200 μm (made of HUVEC, 3T3, and 4T1 cells) (Fig. 3A4). Moreover, we also demonstrated the bioprinting of green fluorescent protein (GFP)-labeled MSC spheroids in the shape of triangle and ring into other gels, including type I collagen (COL I) and gelatin methacryloyl (GelMA), as shown in Fig. 3 (A5 and A6, respectively). To highlight the unprecedented precision of AAB, we bioprinted eight different-sized MSC spheroids on top of each other without any gel support (Fig. 3, A7 and A8) and also fabricated a hollow bridge shape with MSC spheroids using the same approach (fig. S6, B1 and B2). Moreover, we demonstrated another example of a hollow bridge configuration, where the middle spheroid in the second layer was supported by the underlying gel without any spheroid support underneath (fig. S7). This was accomplished by bioprinting the gel and spheroids alternately at each layer, which necessitated the precise control of gel thickness; however, the gel thickness was dependent

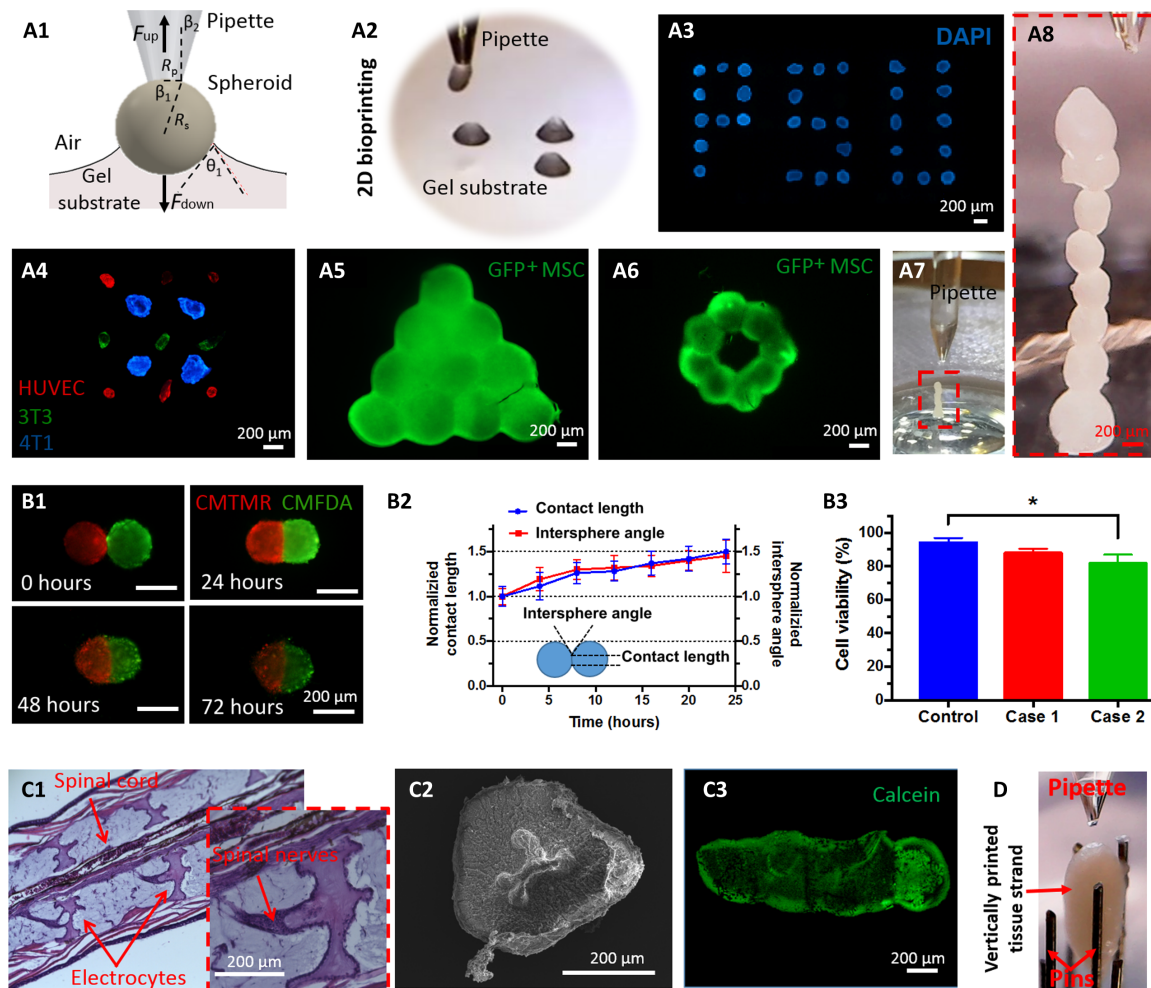


Fig. 3. Patterning and bioprinting of a wide range of biologics. (A1) A schematic showing critical parameters during bioprinting. (A2) An image from the traveling camera showing spheroid placement onto a gel substrate. Fluorescent images showing (A3) PSU and (A4) matrix patterns. GFP⁺ MSC spheroids were patterned onto (A5) COL I and (A6) gelatin-methacryloyl (GelMA). (A7 and A8) Images showing that eight fixed spheroids were bioprinted on top of each other in air without any gel support during bioprinting. DAPI, 4',6-diamidino-2-phenylindole. (B1) Time-lapse images of self-assembly process after bioprinting of 1-day cultured 3T3 spheroids at 0, 24, 48, and 72 hours (B2) and the normalized contact length and intersphere angle of fusing spheroids up to 24 hours. (B3) Cell viability of 3T3 spheroids that were not treated with bioprinting (control), after bioprinting inside the cell media (case 1), and after bioprinting into a gel substrate (case 2) ($n = 3$; $*P < 0.05$). CMTMR, 5-(and-6)-(((4-chloromethyl)benzoyl)amino) tetramethylrhodamine; CMFDA, 5-chloromethylfluorescein diacetate. (C1) Hematoxylin and eosin staining from the sagittal plane of a tail segment of electric fish showing stacked electrocytes in series. (C2) The SEM image of a single electrocyte. (C3) Calcein staining of bioprinted electrocytes. (D) A bio-printed cartilage tissue strand between pins. Photo credit: Bugra Ayan, Penn State University.

on several factors, such as the droplet resolution, cross-linking time, and spreading behavior of droplets, which were not trivial to control at the same time using microvalve bioprinting. To overcome this fundamental limit, self-healing Bingham plastic support gels (35) could be used to freely move the spheroids inside gels, which may bring more flexibility in self-assembly of highly complex geometries including hollowed-out structures.

In addition, self-assembly of spheroids was investigated at pre-determined time points. As shown in Fig. 3B1, 3T3 spheroids were bioprinted into fibrin with close proximity and then cultured for 72 hours. The two individual 3T3 spheroids bioprinted next to each other gradually fused to form a larger spheroid to minimize their surface energy, as described in a previous study (21). The normalized contact length and intersphere angle increased by 50% over the first 24 hours of culture (Fig. 3B2). To evaluate the role of bio-

printing on the viability of spheroids, two cases were evaluated. In case 1, the viability of spheroids was determined immediately after lifting spheroids and depositing them into another cell medium reservoir. In case 2, the viability of spheroids was evaluated after bioprinting them into the gel substrate. Spheroids, which were not subjected to the bioprinting process, were used as a positive control group. The viability of spheroids in the positive control group and case 1 were determined to be ~94 and ~88%, respectively (Fig. 3B3). In case 2, cell viability was measured to be ~82%. The decrease in cell viability could be due to the aspiration force or dehydration during the rapid transfer or cell damage when spheroids were submerged into the hydrogel substrate; however, viability levels over 80% for bioprinting of spheroids could still be considered moderate, as viability of fabricated cells aggregates even without bioprinting could be in that range (36).

In addition to bioprinting of spheroids, the AAB system also enabled the bioprinting of other biologics. For example, we demonstrated the bioprinting of electrocytes isolated from electrogenic organs of electric fish. Because of the asymmetric functionality of their anatomy and their spatial arrangements in series configuration in an electric organ (similar to batteries connected in series; Fig. 3C1), electrocytes produce a considerable amount of electricity (37). In this study, five electrocytes (~400 μm in diameter; Fig. 3C2) from weakly electric fish (*Brachyhypopomus gauderio*) were obtained according to the animal protocol (Institutional Animal Care and Use Committee #47870) and patterned next to each other onto agarose using AAB with a back pressure of ~20 to 25 mmHg (Fig. 3C3). To the best of our knowledge, this is the first bioprinting of electrocytes, which can be used in biofabrication of biological batteries for various applications—such as pacemakers, cochlear implants, and brain chips—in the future (38). In addition, these cells could be arranged in the form of biological circuits for biocomputing or as bioelectric interfaces for use in treating limb loss, musculoskeletal disorders, and body augmentation as well as cyborg organs interfacing electrical devices and biology (39). The presented approach showed the

possibilities of bioprinting not only spheroids or single cells but also irregularly shaped aggregates. For example, Fig. 3D shows vertical bioprinting of tissue strands [described in our previous work (5)] into the space between pins, which can be used for fabrication of scalable tissues of muscle, fat, cartilage, nerves, blood vessels, etc.

To demonstrate other unique capabilities of the presented approach, heterogeneous tissue complexes were 3D bioprinted using spheroids of different sizes and types including tdTomato⁺ HUVEC spheroids (~155 μm) and GFP⁺ MSC spheroids (~390 μm) (Fig. 4, A and B). Spheroids were arranged into a pyramid structure to clearly visualize the heterogeneous architecture using confocal imaging, where alginate was used as a sacrificial gel and the first, second, and third layers constituted of HUVEC, MSC, and HUVEC spheroids, respectively. This example clearly demonstrates the unique deposition ability of the AAB technique, as the last HUVEC spheroid was accurately placed into the small and confined space between three adjacent MSC spheroids (~2.5-fold of HUVEC spheroid size) on the third layer. Alginate preserved the structural integrity of the bioprinted pattern during the initial stage of culture. Moreover, it enabled the bioprinted entities to stick in their precise locations,

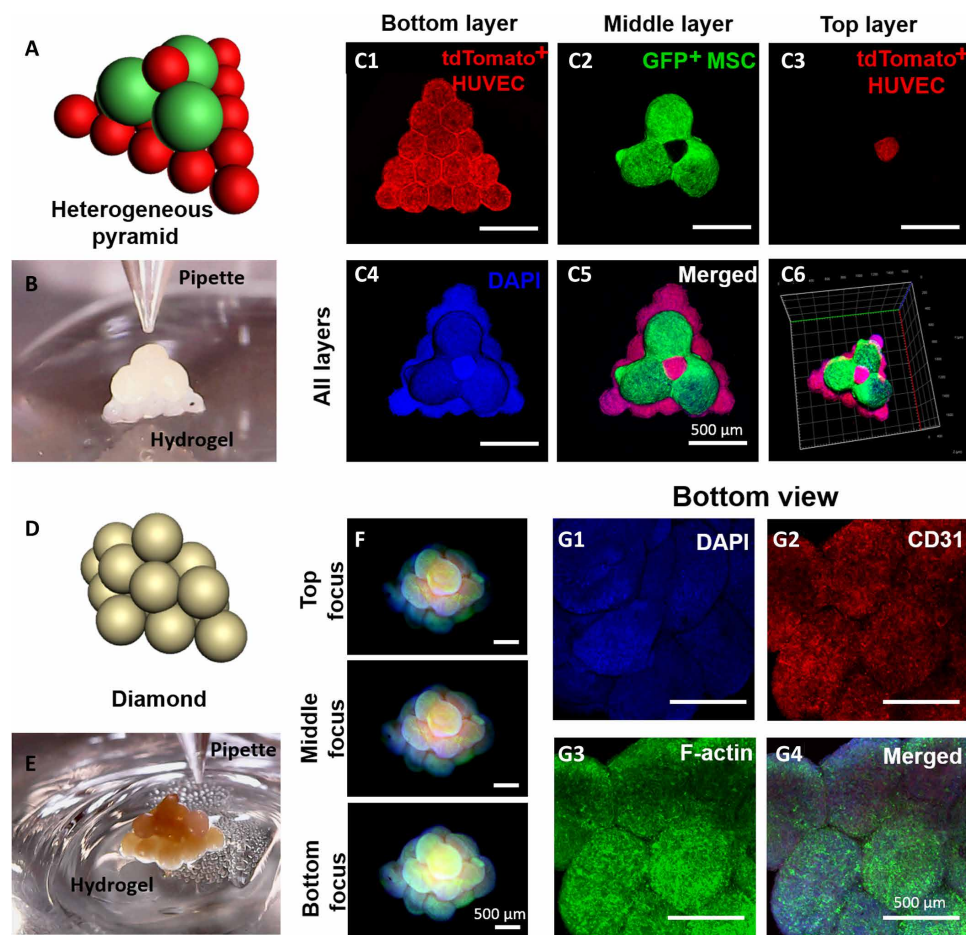


Fig. 4. 3D bioprinting of spheroids. (A) A schematic illustration of 3D bioprinting of a heterogeneous pyramid construct using different sizes and types of spheroids. (B) A photograph of the bioprinted three-layer heterogeneous pyramid. (C1 to C6) 3D reconstruction of confocal images of bioprinted pyramid of tdTomato⁺ HUVEC spheroids (first and third layers) and GFP⁺ MSC spheroids (second layer). (D) A schematic illustration of a diamond construct made of MSC/HUVEC spheroids. (E) A photograph showing 3D bioprinted diamond from the side camera. (F) Fluorescent images of the bioprinted diamond, which were stained with DAPI, CD31, and F-actin. (G1 to G4) Confocal images of the diamond construct (bottom view) (note that 1-day cultured HUVEC and 2-day cultured MSCs were used in these experiments). Photo credit: Bugra Ayan, Penn State University.

which were defined before the bioprinting process. To print the sacrificial alginate, we used a unipolar wave pulse with a dwell voltage (amplitude) of 5 V and a dwell time (valve opening duration) of 1000 μ s for actuating the microvalve dispenser, where a positive back pressure of \sim 103 kPa was used for driving the flow of sodium alginate inside the tubing. The reader is referred to fig. S8A for the optimization of dwell time and droplet volume. Afterward, sodium alginate layer was partially cross-linked with aerosol form of CaCl_2 for 30 s, and spheroids were bioprinted as explained in Fig. 1. Patterned spheroids were partially fused and maintained their initial position after 48 hours of incubation. After 2 days of culture, alginate was gently dissolved [using an alginate lyase as explained in our earlier work (5)], and the bioprinted constructs maintained their integrity even after the sacrificial alginate was removed. As evident from the confocal images (Fig. 4, C1 to C6), spheroids were well connected in 3D. A similar arrangement was also presented with MSC spheroids of three different dimensions, where spheroids got larger as more layers were laid down (fig. S9, A to C). We also demonstrated a more complex pattern such as a 3D diamond pattern with MSC/HUVEC spheroids (Fig. 4, D to G). To the best of our knowledge, this is the first bioprinting of tissue spheroids with such a positional accuracy, \sim 15% with respect to the spheroid size, yielding highly intricate geometries and heterogeneous structures in 3D.

Applications of AAB technology

In this study, we have demonstrated the utilization of AAB in both scaffold-based and scaffold-free configurations and presented two unique applications demonstrating its potential in the development of physiologically relevant culture environments for studying angiogenic sprouting and fabrication of osteogenic tissues for tissue engineering purposes. To demonstrate the application of AAB in scaffold-based fabrication of physiologically relevant culture environments, we bioprinted HUVEC spheroids into fibrin hydrogel with a predetermined distance apart and studied their collective angiogenic sprouting behavior. This importantly signifies that angiogenic sprouting behavior can be tailored by varying the proximity of spheroids, hence directly affecting cell-cell signaling. To study the effect of distance on angiogenic sprouting, we deposited droplets of fibrinogen (6 mg/ml) [loaded with HDFs (0.5 million/ml)] and thrombin (2.4 U/ml) layer by layer (in 1:1 volume) to fabricate fibrin constructs, as such concentration ranges support angiogenesis of HUVECs (40). A positive back pressure of \sim 103 kPa was used for driving the flow of fibrinogen and thrombin solutions inside the tubing and dispenser. To dispense a ratio of 1:1 of fibrinogen and thrombin, we used dwell times of 500 and 700 μ s for obtaining the same droplet volumes at the microvalve dispensers, respectively. The reader is referred to fig. S8 (B and C) for the optimization of droplet generation for fibrinogen and thrombin solutions. HUVEC spheroids were then bioprinted into fibrin before complete gelation. The distances between the spheroids were maintained at 400 ± 10 , 800 ± 13 , and 3000 ± 16 μ m (isolated spheroids used as a control group) (Fig. 5A1). Bioprinted constructs were cultured for a period of 7 days. Angiogenic sprouting from HUVEC spheroids at days 2, 5, and 7 was quantified using AngioTool software (41). Spheroids with close proximity to each other were seen to have higher total vessel length as compared to isolated spheroids right from the initial stages of culture. The combined length of sprouts was 13 and 11 mm for 400 and 800 μ m, respectively, as compared to the control group, which were around 6 mm (Fig. 5A2). A similar trend was also

observed for the total vessel area. There was approximately 3- and 2.5-fold increase in the vessel area for 400- and 800- μ m distances on day 7 as compared to the control group, respectively. Although the total number of branching points or junctions was not significantly different among different groups at day 2, the sprouts branched more when spheroids were bioprinted close to each other, as compared to the control group (fig. S10). On day 7, the number of junctions for 400- and 800- μ m distances was 2.1- and 1.7-fold greater than those for the control group, respectively. The mean lacunarity refers to the amount of free space around the sprouted capillaries, and an increase in angiogenic sprouting results in a decrease in lacunarity (42). This yields a measurement of the sprouting activity, and the mean lacunarity was the highest for the control group compared to other two groups.

In our study, HUVEC spheroids bioprinted with 400- and 800- μ m distances apart were considered to be in close proximity. On the other hand, HUVEC spheroids bioprinted with 3000- μ m distance apart were far enough to be considered “isolated spheroids” (control group). Proximity between cells triggers a cascade of events that, in turn, influences cellular behavior, and to study these events, it is important to control localization under *in vitro* conditions (43). The presented approach offers the capability of controlling the distance between spheroids and thus aims to better understand this signaling between spheroids. Sprouting properties such as vessel length, junction formation, and vessel area were all enhanced when spheroids were close to each other as compared to when they were placed far apart. The presence of HDFs in the matrix surrounding HUVEC spheroids also reinforced the formation of stable sprouts. It is known that fibroblasts act as supporting cells and surround the capillary-like structures, which gradually develop by self-organization of endothelial cells and simultaneous degradation of fibrin matrix (44). Moreover, fibroblasts secrete various soluble growth factors such as vascular endothelial growth factor (VEGF), angiopoietin-1, platelet-derived growth factor (PDGF) (45, 46), which enhance and modulate the growth of angiogenic sprouts (47). Bioprinted HUVEC spheroids close to each other probably up-regulated the combined secretion of these growth factors in the vicinity of the spheroids, which led to enhanced sprouting properties. The sprouts from closely placed spheroids extended toward each other and gradually fused to form a capillary network.

To better understand whether the positioning of spheroids affected their collective angiogenic sprouting behavior, GFP⁺ and tdTomato⁺ HUVEC spheroids were bioprinted into fibrin gel (with same properties as discussed before) at 400-, 800-, and 3000- μ m distances apart, and cultured over a period of 7 days (Fig. 5B1). A directionality analysis was then performed to investigate the role of the presence of a nearby spheroid on the directionality of angiogenic sprouting. Thus, the angle made by each sprout with the horizontal line (0°/180°) was measured for all spheroids. The angle spans [60°, –60°] for GFP⁺ HUVEC and [120°, 240°] for tdTomato⁺ HUVEC spheroids, where sprouts primarily grew toward the other spheroid, were considered the angles of interest (AOIs), as highlighted in Fig. 5B2. On day 7, the percentage of normalized number of sprouts (where the total number of sprouts were normalized with respect to the total angle span) in AOI was significantly higher than that of the other angle span (indicated with “Other”) for 400- and 800- μ m distances, indicating a dominating directionality of angiogenic sprouting toward the other spheroid. The percentage of normalized number of sprouts for AOI was \sim 63 and 65 for GFP⁺ and \sim 59 and 61 for

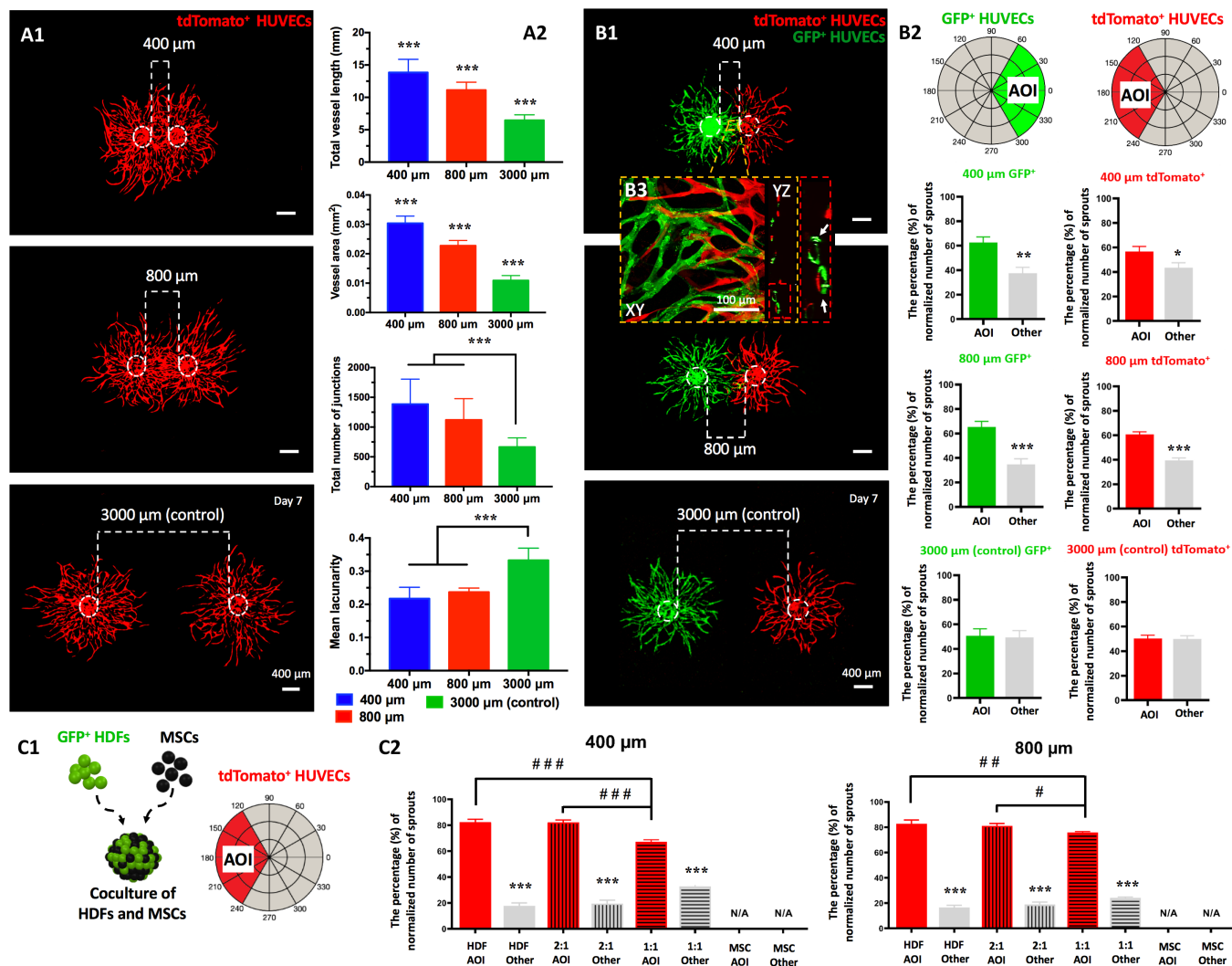


Fig. 5. Bioprinting of physiologically relevant culture environments to study the angiogenic sprouting behavior of HUVEC spheroids. (A1) Epifluorescent images of bioprinted tdTomato⁺ HUVEC spheroids with varying distances (400 to 3000 μm) apart on day 7. (A2) Graphical representation of various sprouting properties—namely, total vessels length, total number of junctions formed, vessel area, and mean lacunarity—obtained at day 7 for bioprinted HUVEC spheroids ($n = 3$; $***P < 0.001$). (B1) Epifluorescent images of bioprinted GFP⁺ and tdTomato⁺ HUVEC spheroids with varying distances (400 to 3000 μm) apart on day 7 along with higher-magnification confocal images of the interface region in XY and YZ planes showing capillaries formed by both GFP⁺ and tdTomato⁺ HUVECs (indicated by white arrows). (B2) Directionality analysis demonstrating the direction and percentage of normalized number of sprouts on day 7 ($n = 3$; $*P < 0.05$, $**P < 0.01$, and $***P < 0.001$) [note that green and red bars demonstrate the angles of interest (AOIs), which are $[60^\circ, -60^\circ]$ for GFP⁺ HUVECs and $[120^\circ, 240^\circ]$ for tdTomato⁺ HUVECs]. (B3) Confocal images at the interface of two spheroids showing capillaries formed by both GFP⁺ and tdTomato⁺ HUVECs. (C1) A schematic illustration of the directionality of sprouts from a HUVEC spheroid toward a spheroid of GFP⁺ HDF and MSC cocultures. (C2) The directionality analysis for different mixing ratios of HDF:MSC, including HDF (control), 2:1, 1:1, and MSC (control), on day 7 ($n = 3$; $***P < 0.001$ shows significance between AOI and “Other” for each group, and $\#P < 0.05$, $\##P < 0.01$, and $\###P < 0.001$ show significance among AOIs of different groups) [note that N/A represents the none applicability of the directionality analysis, as no sprouts were observed in the MSC-only group; no directionality analysis was performed for the 3000-μm distance, as sprouting was not observed and HUVECs exhibited spreading only; 1-day cultured HUVECs were used in all experiments; and the critical lifting pressure for coculture HDF/MSC spheroids (2:1 and 1:1 ratio) was determined to be 28.7 and 29.1 mmHg, respectively, through interpolation of the critical lifting pressure values for HDF and MSC spheroids presented in Fig. 2F].

tdTomato⁺ HUVEC spheroids, for 400- and 800-μm distances, respectively. Although the directionality of sprouts for all cases may not be very apparent on day 2 (initial stages of culture; fig. S11, A1 and A2), on day 5 (later stages of culture; figs. S11, B1 and B2, and S12), mature sprouts were more concentrated within AOI. In addition, for sprouts formed in directions falling outside the AOI (depicted in gray), we observed more random growth of sprouts over time. The sprouts for spheroids that were 3000 μm apart were random and did not indicate any directionality from days 2 to 7

(Fig. 5B2, bottom, and fig. S12C). For 400-μm distance, it was also observed that the GFP⁺ HUVECs suppressed the sprouting ability of tdTomato⁺ HUVECs day 2 onward, where higher numbers of GFP⁺ HUVEC sprouts were observed at the interface [see fluorescent images in fig. S11 (A1 to B1)]. Domination of GFP⁺ HUVEC sprouts could be due to the fact that GFP⁺ HUVECs in this experiment were from an earlier passage (passages 2 to 5) with respect to tdTomato⁺ HUVECs (passages 5 to 7) (48). In addition, we investigated whether sprouts from both spheroids interacted and thus

performed confocal imaging at the interface close to the tdTomato⁺ HUVEC spheroid (Fig. 5B3). We noticed that some capillaries were formed by both GFP⁺ and tdTomato⁺ HUVECs, as shown by arrows, which could be due to vascular anastomosis or the migration of GFP⁺ HUVECs to the other side of the interface and their contribution to the capillary formation by tdTomato⁺ HUVECs spheroids. Overall, the results showed that HUVEC spheroids bioprinted close to each other influence each other's sprouting behavior, which led to a well-organized network formation between the sprouting bodies.

In the abovementioned experiments, we investigated the role of multiple HUVEC spheroids on their collective sprouting behavior, where HDFs were bioprinted as a single-cell suspension in fibrin, had direct contact with HUVEC spheroids, acted as supporting cells, and aided in forming stable sprouts. To explore whether HDFs could still influence the sprouting behavior of HUVECs even when they were not in direct contact with HUVECs, we reconfigured the design of the experiments presented above. In this regard, a HUVEC spheroid was bioprinted along with a coculture spheroid of GFP⁺ HDFs and MSCs (with controlled distance apart), which enabled us to change the concentration of HDFs and study the differential effect of coculture composition on HUVEC sprouting. GFP⁺ HDF/MSCs spheroids, in 2:1 and 1:1 ratios, were bioprinted next to tdTomato⁺ HUVEC spheroids in fibrin with the same properties as discussed before (Fig. 5C1). HDF and MSC (homocellular) spheroids were used as control groups. The distance between these spheroids was varied from 400 to 3000 μ m, as performed before. For the cases of 400 and 800 μ m, HUVECs were attracted toward spheroids of HDF, 2:1, and 1:1 groups and were seen arranging into sprouts over a period of 7 days (figs. S13 and S14). The directionality analysis on day 7 revealed that the percentage of normalized number of sprouts within AOI for HDF, 2:1, and 1:1 groups for 400- μ m distance were ~82, 80, and 67, respectively (Fig. 5C2). For 800- μ m distance, a similar directionality was observed, where the percentage of normalized number of sprouts within AOI for HDF, 2:1, and 1:1 groups were determined to be ~84, 81, and 76, respectively. On the other hand, spheroids in the MSC group (Fig. 5C2) or spheroids located apart with a 3000- μ m distance (fig. S15) did not induce sprouting day 2 onward; rather, HUVECs exhibited spreading behavior. On day 2, for the case of 800 μ m, although the tip cells from HUVEC spheroids were not observed to have any physical contact with HDFs at the interface of both spheroids, sprout-like structures were already formed (fig. S16A). These structures were directed toward HDFs, as the relevant directionality analysis revealed a significant difference between AOI and Other for HDF, 2:1, and 1:1 groups (fig. S16B). This could be due to the fact that HDFs communicated with HUVECs via paracrine signaling by the possible diffusion of secreted growth factors, such as VEGF, angiopoietin-1, and PDGF, as discussed before (45, 46). By day 5 when HDFs substantially migrated out of the coculture spheroids, HDFs interacted with HUVECs outside AOI, particularly within angle spans [60°, 120°] and [240°, 300°], and induced sprout formation in those directions (fig. S17). Overall, more stable sprouts were observed in HDF-involved spheroids, and the results revealed that better directionality of angiogenic sprouting could be attained when the density of HDFs increased in the coculture spheroid. The presence of MSCs, on the other hand, had a negative impact on angiogenic sprouting of HUVECs, which could be due to the inhibitory effect of MSCs on the angiogenic potential of HUVECs via cell-cell contact through modulation of the VE-cadherin/ β -catenin signaling pathway as described before (49, 50).

To demonstrate another major application of AAB, osteogenic tissues were bioprinted using MSC/HUVEC spheroids as building blocks in a scaffold-free configuration. After fabrication, two different osteogenic differentiation culture strategies were used, both with equal total exposure time of osteogenic induction. This was performed to decode the role of midterm osteogenic induction of stem cell-based spheroids (before bioprinting) on the mineralization and assembly behavior of generated tissues (fig. S18). In strategy no. 1, 2-day cultured spheroids were bioprinted into a triangle pattern (Fig. 6A). After bioprinting, triangle-shaped tissue complexes maintained their integrity and transformed into a more compact and dense structure after 3 days in proliferation culture conditions [growth media (GM)]. Spheroids in this triangle-shaped pattern self-assembled over time, where cells exhibited a viability of 83% after 5 days of incubation, and the assembled structure was further cultured for a period of 12 days in osteogenic media (OM) (Fig. 6, B and C). In general, MSCs cultured in OM express high levels of osteogenic markers (51). To confirm the osteogenic differentiation of bioprinted tissues, the early osteogenic differentiation marker, Runx-related transcription factor 2 (RUNX2), was used for immunohistochemical staining. At the same time, the presence of HUVECs was confirmed by CD31 staining. As shown in Fig. 6D, bioprinted tissues expressed osteogenic- and endotheliogenic-specific markers, as indicated by positive staining of RUNX2 and CD31. Calcium deposition of osteogenically differentiated tissues was also confirmed by Alizarin red staining. As shown in Fig. 6E, substantial calcium deposition was observed after 12 days of osteogenic induction, particularly at the core of the assembled tissue. As substantial contraction was observed after the fusion of MSC/HUVEC spheroids and the originally bioprinted triangular shape was not maintained (Fig. 6C) as well as the mineralization was not uniform throughout the tissue boundary (Fig. 6E), we also followed an alternative strategy (strategy no. 2) to preserve the bioprinted shape of osteogenic tissues (fig. S18). In this regard, MSC/HUVEC spheroids were first maintained in GM for 5 days, followed by inducing them with OM for 10 days. Next, spheroids were bioprinted and then kept for another 2 days in OM. In both strategies, the total exposure time to GM and OM was identical. At the end of culture (Fig. 6F), bioprinted tissues using strategy no. 2 exhibited strong expression of RUNX2 with more uniform distribution of mineralization demonstrated by Alizarin red staining, although RUNX2 staining was stronger in cores of spheroids (Fig. 6, G to J). Intensity analysis of RUNX2 revealed that RUNX2 staining was the strongest in the core of tissues or at the interface between spheroids and the weakest on the surface of the assembled tissues (Fig. 6, K and L, and fig. S19A), while CD31 staining was uniformly distributed throughout the histological sections of bioprinted tissues under both strategies (fig. S19B). A previous study demonstrated that HUVEC-mediated paracrine factors, including VEGF and the inflammatory mediator prostaglandin E₂ (PGE₂), promoted the osteogenesis of periodontal ligament stem cells under hypoxic conditions regulated by mitogen-activated protein kinase (MAPK) kinase/extracellular signal-regulated kinase and p38 MAPK pathways (52). As the core of tissues and interface between spheroids were more hypoxic compared to the surface of assembled tissues, the osteogenic differentiation of MSCs could be further advanced in those regions by PGE₂ and VEGF paracrine factors secreted by HUVECs. In addition, limited shape change was observed. This could be due to the fact that MSCs in MSC/HUVEC spheroids, cultured in OM for 10 days before bioprinting, were in the osteogenic differentiation pathway and their proliferation capability was diminished as reported

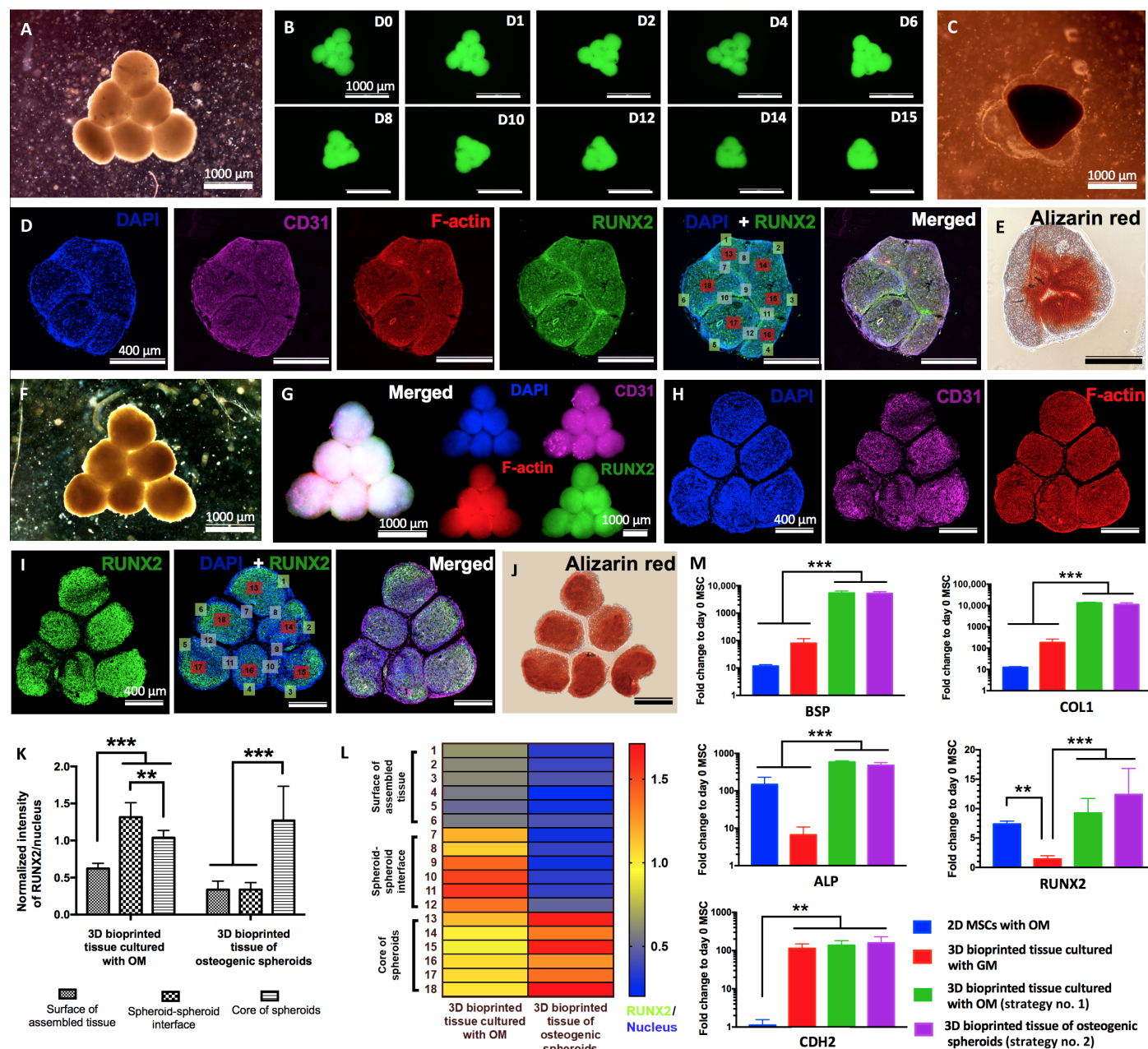


Fig. 6. Biofabrication of osteogenic tissues. Strategy no. 1: (A) Triangle-shaped tissue complexes were bioprinted using MSC/HUVEC spheroids and cultured for 3 days in GM and 12 days in OM. (B) Time-lapse images showing fusion of GFP⁺ spheroids up to day 15 (D15) after bioprinting. (C) An optical image showing the assembled tissue at day 15 after bioprinting. (D) Immunofluorescence staining (DAPI, CD31, F-actin, RUNX2, and DAPI + RUNX2) and (E) Alizarin red staining of the sectioned tissue. Strategy no. 2: (F) The final shape of the bioprinted tissue of osteogenic spheroids (cultured for 10 days in OM before bioprinting and 2 days in OM after bioprinting). Immunofluorescent images of (G) the bioprinted tissue and (H) confocal images of its histological sections stained for DAPI, CD31, and F-actin and (I) RUNX2 and DAPI + RUNX2. (J) Alizarin red staining of the tissue section. (K) Quantification of normalized RUNX2 intensity at different regions including the surface of assembled tissue, spheroid-spheroid interface, and core of spheroids ($n = 50$; $**P < 0.01$ and $***P < 0.001$). (L) A representative heat map figure showing RUNX2/DAPI distribution in the surface of assembled tissue, spheroid-spheroid interface, and core of spheroids for strategy nos. 1 and 2. (M) *BSP*, *COL1*, *ALP*, *RUNX2*, and *CDH2* gene expressions of 2D MSCs cultured in OM (control), 3D bioprinted tissues cultured in GM (control), and 3D bioprinted tissues cultured using strategy nos. 1 and 2 ($n = 5$; $**P < 0.01$ and $***P < 0.001$).

in a previous study (53), and hence, limited contraction was observed in spheroids. Another advantage of strategy no. 2 is that the culture duration after bioprinting was reduced, where 2-day cultured tissues after bioprinting were still structurally stable. We also analyzed the

expression levels of bone sialoprotein (*BSP*), type I collagen (*COL1*), alkaline phosphatase (*ALP*), *RUNX2*, and *CDH2* (N-cadherin) genes for both strategies, and bioprinted tissues cultured in GM (labeled as “3D bioprinted tissue cultured with GM”) and MSCs differentiated

in 2D for 12 days (labeled as “2D MSCs cultured with OM”) were used as control groups. As shown in Fig. 6M, expression levels of *BSP*, *COL1*, *ALP*, and *RUNX2* genes for both strategies were similar to each other and significantly higher than those of control groups. In addition, the expression level of *CDH2* gene (encoding N-cadherin protein) for all 3D bioprinted tissue groups were similar to each other and higher than that of the 2D control group. Overall, by changing the osteogenic induction window under the same total osteogenic induction duration, the shape of bioprinted tissues and uniformity of mineralization could be controlled, although no differences were detected in the expression levels of osteogenic genes.

CONCLUSIONS AND OUTLOOK

Together, we demonstrated the ability of AAB approach to bioprint a wide range of biologics, which can allow one to explore a myriad of avenues such as tissue-tissue interactions, tissue-material interactions, and angiogenesis in the rapidly growing field of tissue engineering and regenerative medicine. In addition, AAB provides an outstanding platform for the bottom-up assembly of various spheroids having diverse applications in tissue engineering. Precise positioning of spheroids can also be critical for applications such as building organ-on-a-chip devices or microphysiological systems where the proximity of spheroids to each other or a perfusion channel can be crucial for the viability and function of spheroids as well as the robustness of the developed system. Organoids or spheroids are currently loaded using manual approaches, which may reduce the repeatability of system outcome measurements (such as measured insulin in circulating perfusion media in a pancreas-on-a-chip model) (9). To the best of our knowledge, the presented approach is the first bioprinting method that allows high-precision bioprinting of spheroids in both scaffold-free and scaffold-based manner. In addition, the underlying mechanism explaining the physical behavior of viscoelastic spheroids and their interactions with physical governing forces during aspiration, lifting, and bioprinting has not been documented in literature to date, and with our custom-made bioprinter, we were able to exploit it for multiple applications enumerated throughout this paper. In particular, mediating angiogenic sprouting and its directionality through precise positioning of spheroids in a gel medium and the impact of paracrine signaling in response to such positioning has not been presented elsewhere. Besides, the role of midterm osteogenic induction to stem cell-based spheroids (before bioprinting) on the mineralization and assembly behavior has not been reported before. Therefore, the presented bioprinting approach can be used in detailed understanding of fundamental biology and studying angiogenesis, histogenesis, and organogenesis.

In conclusion, we propose a more effective strategy of AAB system, taking advantage of a simple-to-use, cost-effective (<\$1000), and reproducible tissue bioprinting platform, which can be useful in a wide variety of applications, including but not limited to organ-on-a-chip devices, drug testing devices, microfluidics, in vitro human disease models, organoid engineering, biofabrication and tissue engineering, biocomputing, and biophysics. However, our AAB system requires further improvement to increase the time effectiveness in fabrication of scalable tissues. In the near future, our AAB platform could be advanced to be able bioprint an array of spheroids simultaneously for scale-up tissue fabrication in a shorter time.

MATERIALS AND METHODS

Materials

Sodium alginate solution was made by dissolving 1% (w/v) sodium alginate (Sigma-Aldrich, UK) in deionized (DI) water. Calcium chloride solution was prepared by dissolving 4% (w/v) calcium chloride (CaCl_2) (Sigma-Aldrich, St. Louis, MO) in DI water. For constructing fibrin scaffolds, fibrinogen (6 mg/ml) (Sigma-Aldrich) and thrombin (2.4 U/ml) (Sigma-Aldrich) were prepared for microvalve bioprinting. For bioprinting of electrocytes, agarose (A20070-100, Research Products International, IL) was dissolved in DI water to obtain a solution of 1% (w/v) agarose at 90°C. COL I was extracted from rat tails according to a published protocol (54). GelMA was synthesized according to an established protocol (55). Detailed preparation methods of both materials can be found in the Supplementary Materials.

Cell preparation

The mouse fibroblast cell line, 3T3, and the mouse mammary carcinoma line, 4T1, were obtained from the laboratory of A. Mastro, PSU (State College, PA). Culture media for 3T3 fibroblasts composed of Dulbecco's modified Eagle's medium (DMEM) (Corning, Manassas, VA), supplemented with 10% fetal bovine serum (FBS) (Life Technologies, Grand Island, NY) and 1% penicillin-streptomycin (Corning). 3T3 cells were used at passages 22 through 27. 4T1 cells were grown in RPMI (Corning), 10% FBS, 1% penicillin-streptomycin. Passages 7 through 12 were used for 4T1 cells. HUVECs were purchased from Lonza and cultured in MCDB 131 base media (Corning) supplemented with 10% FBS (Corning), 1% glutamine (Gibco, Life Technologies), 0.5% bovine brain extract (Lonza, Walkersville, MD), heparin (10 U/ml) (Sigma-Aldrich), endothelial cell growth supplement (3 mg/ml) (Sigma-Aldrich), and 1% penicillin-streptomycin (Corning). HUVECs were used at passages 3 through 8. HUVECs were also transduced in house with EF1 tdTomato lentivector (Vectalis, Toulouse, France) to ease cell visualization for fluorescence microscopy according to the manufacturer's instructions. GFP⁺ HUVECs were purchased from Angio-Proteomie (cAP-0001GFP; Boston, MA) and were used at passages 2 through 5. HDFs, obtained from N. Zavazava's laboratory at The University of Iowa (Iowa City, IA), were cultured in DMEM supplemented with 10% FBS (Corning), 1% glutamine (Gibco), 1% sodium pyruvate (Gibco), and 1% penicillin-streptomycin (Corning). HDFs were used at passages 7 through 12. GFP⁺ HDFs were purchased from Angio-Proteomie (cAP-0008-adGFP; Boston, MA) and were used at passages 2 through 6. MSCs were obtained from Lonza (Walkersville, MD) and RoosterBio (Frederick, MD) and cultured in SU-005 RoosterBasal-MSC (RoosterBio). Passages 4 through 8 were used for MSCs. GFP⁺ MSCs were purchased from Cyagen, cultured in SU-005 RoosterBasal-MSC (RoosterBio), and used at passages 2 through 6.

All cells were maintained at 37°C in a 5% CO₂ humidified atmosphere. Cell culture medium was changed every 2 to 3 days. Subconfluent cultures were detached from the flasks using a 0.25% trypsin-0.1% EDTA solution (Life Technologies) and split to maintain cell growth.

Fabrication of tissue spheroids

Adherent cultures of each cell type were detached from the culture vessels with 0.25% trypsin-EDTA (Life Technologies, Grand Island, NY) solution. Trypsin was neutralized with appropriate GM, and cells were counted by a hemocytometer. Each cell type was then

diluted to a concentration of 2500, 5000, and 10,000 cells in 200 μ l of appropriate GM. The cell suspension (200 μ l) was then pipetted into a single well of a U-bottom 96-well microplate with a cell-repellent surface (Greiner Bio-One, Monroe, NC). For fabrication of MSC/HUVEC spheroids made of 50,000 cells, MSCs and HUVECs were combined at a ratio of 92:8. The microplates were then incubated at 37°C in a 5% CO₂ humidified atmosphere. Spheroid formation was monitored daily on an EVOS FL cell imaging system (Life Technologies). For fabrication of GFP⁺ HDF/MSC coculture spheroids, 5000 cells were used in total, and GFP⁺ HDFs and MSCs were cocultured in ratios of 2:1 and 1:1 for 1 day. During the fabrication and culture of HUVECs spheroids, EGM-2MV medium (Lonza) was used.

Scanning electron microscopy

Field-emission SEM (FEI Nova NanoSEM 630) was used to investigate the surface topography of fabricated spheroids and dissociated electrocytes (see the Supplementary Materials for dissociation of electrocytes). Spheroids were harvested after 2 days of culture. Spheroids and electrocytes were fixed in 4% paraformaldehyde (Sigma-Aldrich) overnight; samples were then carefully washed in phosphate-buffered saline (PBS) and dehydrated using graded ethanol solutions (25 to 100%). To ensure complete removal of water, samples were further dried in a critical point dryer (CPD300, Leica EM, Wetzlar, Germany). On complete dehydration, they were sputter-coated with iridium (Leica) and imaged at an accelerating voltage of 3 to 5 keV.

Hydroxyproline assay

A total of 1000 2-day cultured spheroids of each type (with ~2500 cells per spheroid) were collected and homogenized in 100 μ l of distilled water. Then, 100 μ l of cell homogenate was transferred to a 2-ml pressure-tight vial, added with 100 μ l of 12 M hydrochloric acid, and hydrolyzed at 120°C for 3 hours. The total collagen amount per spheroid type was quantified using a hydroxyproline colorimetric assay kit (BioVision Inc., CA) according to the manufacturer's instructions. Collagen amount expressed by each spheroid type was determined using a PowerWave X-340 spectrophotometer (BioTek, Winooski, VT) at 560 nm, and the results were normalized to the collagen amount expressed by HUVEC spheroids at day 2. Experiments were repeated four times.

Development of the aspiration-assisted bioprinter

Bioprinting of spheroids was used with a MakerBot Replicator 1 3D printer (MakerBot, NY). The extrusion head was removed, and a holder for a pipette and two microvalve heads was 3D-printed using an Ultimaker 2 (Ultimaker) 3D printer. To control the 3D motion stage, a smoothie board (Uberclock, OR) was integrated. The reader is referred to the Supplementary Materials for the details on the construction of the AAB platform.

For fabrication of support constructs, microvalves (INKX0517500A, Lee Company, Bashville, TN) with 250- μ m nozzles (INZA3100914K, Lee Company) were integrated on the bioprinter head. To operate microvalves, a control board (IECX0501350A, Lee Company) was used, which was controlled using Arduino Uno (Arduino, Italy). To cross-link sodium alginate, a portable ultrasonic humidifier (CZHD20, Comfort Zone, China) was used to generate the aerosol form of CaCl₂. Details about the bioprinter setup—including the computer aided design model (fig. S1D), block diagram (fig. S1E), and computer interface (fig. S20)—can be found in the Supplementary Materials.

Surface tension measurement

Spheroids were collected into a petri dish from U-bottom 96-well plates, and then, their surface tension was measured using a micro-pipette aspiration technique, as explained in our recent work (8). Aspirated spheroids were monitored via an STC-MC33USB monochrome camera (Sentech, Japan) equipped with 1-61448 and 1-61449 adaptor tubes (Navitar, Rochester, NY).

Immunostaining and imaging

Spheroids fixed in 4% paraformaldehyde (Sigma-Aldrich) and rinsed in Dulbecco's PBS (DPBS) were stained with NucBlue ReadyProbes reagent (Life Technologies) to visualize the cell nuclei (Fig. 3, A3 and A4); actin cytoskeletal fibers were stained with ActinGreen 488 ReadyProbes reagent according to the manufacturer's instructions. Imaging and 3D reconstruction of a heterogeneous pyramid structure (Fig. 4A) was performed using a Zeiss confocal microscope (LSM 880, Carl Zeiss AG, Oberkochen, Germany) using a 5 \times lens. The 3D reconstruction was obtained using Zen blue software (Carl Zeiss AG). A diamond structure (Fig. 4D) was first imaged through Zeiss Axiozoom (Carl Zeiss AG, Oberkochen, Germany) to capture the entire 3D structure and then further imaged on a confocal microscope (Olympus FV1000, Olympus America Inc., Center Valley, PA) to closely image the DAPI (4',6-diamidino-2-phenylindole), F-actin, and CD31 staining.

Cell viability

Spheroids were removed from the U-bottom well plates and subjected to the bioprinting process. Spheroids directly taken from plates were used as a positive control group. Viability was assessed using a LIVE/DEAD viability assay kit (Life Technologies, Grand Island, NY). Briefly, spheroids were washed twice in DPBS and then placed in the dye solution consisting of 1 μ M calcein acetoxymethyl and 1.6 μ M ethidium homodimer-1 in PBS. Live cells were able to take up and retain the calcein dye, resulting in bright green fluorescence of their cytoplasm. The ethidium homodimer could only enter dead cells where it binds to nucleic acids, producing a bright red fluorescence. Spheroids were imaged at 20- μ m z-stack step size on the Olympus FV1000 confocal microscope with a 60- μ m aperture setting resulting in approximately five to seven images per spheroid. Each image was then analyzed using ImageJ software (National Institutes of Health, USA).

Self-assembly of spheroids

Spheroids made of 3T3 cells were collected from U-bottom 96-well plates and then washed with DPBS twice. CellTracker Orange CMTMR [5-(and-6)-(((4-chloromethyl)benzoyl)amino) tetramethylrhodamine] (Thermo Fisher Scientific) and CellTracker Green CMFDA (5-chloromethylfluorescein diacetate) (Thermo Fisher Scientific, MA) were used according to the manufacturer's instructions. Spheroids were bioprinted with close proximity, and then, images were captured at 0, 24, 48, and 72 hours using EVOS FL Cell Imaging System. The contact length and contact angle of two spheroids were measured every 4 hours up to 24 hours.

Imaging and quantification of endothelial sprouting

Images of sprouting GFP⁺ and tdTomato⁺ HUVEC spheroids at day 7 were taken on the Zeiss Axiozoom microscope at a magnification of $\times 20$ to capture the spheroids bioprinted at various distances. Images of sprouts at days 2 and 5 were taken using the EVOS FL Cell Imaging System. Sprouting behavior of spheroids was analyzed

using AngioTool (41). To obtain the cross-sectional view of the capillary-like structures formed by GFP⁺ and tdTomato⁺ HUVEC spheroids at day 7, samples were imaged using a 40× oil lens on the Olympus FV1000 confocal microscope. For the study with GFP⁺ HDF/MSC coculture and HUVEC spheroids, samples were imaged on the EVOS microscope using fluorescent (4×) channels at days 2 and 5. Images of those samples on day 7 were taken using fluorescent (16× and 40×) and phase (16×) channels by the Axiozoom microscope.

Characterization of osteogenic differentiation

To induce osteogenic differentiation, MSC/HUVEC spheroids were bioprinted and cultured in two different strategies in a custom culture media made of 92% osteogenic differentiation media (Cell Applications Inc., San Diego, CA) and 8% HUVEC culture media. To confirm the morphology of bioprinted tissues undergoing osteogenic differentiation, tissues were sectioned and stained with RUNX2, CD31, F-actin, and DAPI. Cross-sectioned samples were washed three times with DPBS, fixed in 4% paraformaldehyde for 60 min, permeabilized in 0.2% Triton X-100 for 30 min, and blocked with 2.5% normal goat serum (NGS) for 60 min at room temperature. To visualize osteogenic and endothelial-specific genes, the samples were incubated with mouse anti-RUNX2 primary antibody (1:100 in 2.5% NGS) and rabbit anti-CD31 primary antibody (1:100 in 2.5% NGS) for 60 min; washed three times with DPBS; and incubated with goat anti-mouse Alexa Fluor 488 secondary antibody (Molecular Probes; 1:250 in 2.5% NGS) to label RUNX2, goat anti-rabbit Alexa Fluor 647 secondary antibody (Molecular Probes; 1:250 in 2.5% NGS) to label CD31, Alexa Fluor 568 phalloidin (Molecular Probes; 1:1000 in 2.5% NGS) to label filamentous actin, and DAPI (1:1000 in 2.5% NGS) to visualize cell nuclei for 60 min. The stained samples were washed three times with DPBS and imaged by an Olympus FV10i-LIV Confocal Laser Scanning Microscope (Olympus America Inc.) and analyzed using ImageJ software. In addition to sectioned samples, bioprinted tissues were also stained, as a whole-mount sample, as explained above, and fluorescent images were taken on the Zeiss Axiozoom microscope.

To confirm the calcium deposition, cross-sectioned samples were fixed in 4% paraformaldehyde, washed three times with distilled water, and incubated with 2% Alizarin red S stain solution for 30 min at room temperature. Stained samples were washed three times with distilled water and imaged using the EVOS microscope.

To quantify the intensity of RUNX2 and CD31, areas of interest on confocal images were selected using ImageJ. Fifty regions of interest were determined at the surface of the assembled tissue, spheroid-spheroid interface, and core of spheroids on fluorescent images. Each box was used for quantification of the fluorescence intensity. The intensity of RUNX2 and CD31 was normalized by the intensity of DAPI. A representative heat map was generated for the RUNX2/DAPI intensity.

Real-time polymerase chain reaction (PCR) was performed to quantify the gene expression levels of *BSP*, *COL1*, *ALP*, *RUNX2*, and *CDH2*. The primers of the measured mRNA genes were as follows: *BSP* (forward, AAC GAA GAA AGC GAA GCA GAA and reverse, TCT GCC TCT GTG CTG TTG), *COL1* (forward, ATG ACT ATG AGT ATG GGG AAG CA and reverse, TGG GTC CCT CTG TTA CAC TTT), *ALP* (forward, AGC TGA ACA GGA ACA ACG TGA and reverse, CTT CAT GGT GCC CGT GGT C), *RUNX2* (forward, GGT TAA TCT CCG CAG GTC ACT and reverse, CAC

TGT GCT GAA GAG GCT GTT), *CDH2* (forward, GAG CAG TGA GCC TGC AGA TTT T and reverse, TGC TCA GAA GAG AGT GGA AAG CT), and glyceraldehyde 3-phosphate dehydrogenase (*GAPDH*) (forward, ATG GGG AAG GTG AAG GTC G and reverse, GGG GTC ATT GAT GGC AAC AAT A). Real-time PCR was analyzed by using SsoFast EvaGreen Supermix (Bio-Rad, USA), and all results were normalized using *GAPDH*.

Statistical analysis

All data were presented as means ± SD and analyzed by Minitab 17.3 (Minitab Inc., State College, PA, USA) using one-way analysis of variance (ANOVA) to test for significance when comparing the data. Post hoc Tukey's multiple-comparison test was used to determine the individual differences among the groups. Differences were considered significant at **P* < 0.05, ***P* < 0.01, and ****P* < 0.001. For directionality analysis, *t* test was used to compare the results between AOI and Other (where differences were considered significant at **P* < 0.05, ***P* < 0.01, and ****P* < 0.001), and ANOVA (with Tukey's multiple comparison test) was used to compare the results among different groups (where differences were considered significant at #*P* < 0.05, ##*P* < 0.01, and ###*P* < 0.001). Repeated-measures ANOVA (with Tukey's multiple-comparison test) was conducted to compare the results among different days of same groups, and differences were considered significant at **P* < 0.05, ***P* < 0.01, and ****P* < 0.001.

SUPPLEMENTARY MATERIALS

Supplementary material for this article is available at <http://advances.sciencemag.org/cgi/content/full/6/10/eaaw5111/DC1>

Supplementary Materials and Methods

Fig. S1. Aspiration-assisted bioprinter.

Fig. S2. Simulation of aspiration.

Fig. S3. Dimensional and surface tension measurements.

Fig. S4. Compactness of different spheroid types over time.

Fig. S5. Calibration of the pneumatic system and positional precision and accuracy for AAB.

Fig. S6. Bioprinting of tissue spheroids in 2D and 3D.

Fig. S7. Bioprinting of a representative 3D hollow structure.

Fig. S8. Printing parameters for microvalve-based bioprinting.

Fig. S9. A heterogeneous pyramid construct.

Fig. S10. Effect of distance on angiogenic sprouting.

Fig. S11. Effect of distance on the directionality of angiogenic sprouting.

Fig. S12. Directionality analysis of angiogenic sprouting over time.

Fig. S13. Fluorescent and fluorescent/phase images showing angiogenic sprouts from a tdTomato⁺ HUVEC spheroid toward a spheroid of GFP⁺ HDF and MSC coculture in different mixing ratios—including HDF (control), 2:1, 1:1, and MSC (control)—on day 7.

Fig. S14. Fluorescent and fluorescent/phase images showing angiogenic sprouts from a tdTomato⁺ HUVEC spheroid toward a spheroid of GFP⁺ HDF and MSC coculture in different mixing ratios—including HDF (control), 2:1, 1:1, and MSC (control)—on day 7.

Fig. S15. Fluorescent and fluorescent/phase images showing angiogenic sprouts from a tdTomato⁺ HUVEC spheroid toward a spheroid of GFP⁺ HDF and MSC coculture in different mixing ratios—including HDF (control), 2:1, 1:1, and MSC (control)—on day 7.

Fig. S16. Directionality analysis of angiogenic sprouts toward GFP⁺ HDF and MSC coculture spheroids on day 2.

Fig. S17. Directionality analysis of angiogenic sprouts toward GFP⁺ HDF and MSC coculture spheroids on day 5.

Fig. S18. Culture strategies: A schematic of osteogenic culture strategies including strategy nos. 1 and 2.

Fig. S19. Osteogenic tissue biofabrication using strategy nos. 1 and 2.

Fig. S20. Computer interface of AAB.

Table S1. Dynamic contact angles of spheroids at a lifting speed of 5 mm/s.

Table S2. Determination of *F*_{up} and *F*_{down} for bioprinting of various spheroids in 1% (w/v) alginate.

Table S3. Surface tension coefficient of different types of cell media used in our experiments.

Movie S1. Real-time video of spheroid lifting and bioprinting process.

Movie S2. Simulation of spheroid aspiration.

Movie S3. Bioprinting of a tower and a bridge using MSC spheroids in air.

Movie S4. Bioprinting of a tissue strand.

Movie S5. 3D printing of fibrinogen and thrombin via microvalves.

Movie S6. 3D reconstruction of the heterogeneous pyramid construct constituted of tdTomato-labeled HUVEC spheroids on the first and third layers and GFP-labeled MSC spheroids on the second layer.

[View/request a protocol for this paper from Bio-protocol.](#)

REFERENCES AND NOTES

- I. T. Ozbolat, Scaffold-based or Scaffold-free bioprinting: Competing or complementing approaches? *J. Nanotechnol. Eng. Med.* **6**, 024701 (2015).
- V. Mironov, R. P. Visconti, V. Kasyanov, G. Forgacs, C. J. Drake, R. R. Markwald, Organ printing: Tissue spheroids as building blocks. *Biomaterials* **30**, 2164–2174 (2009).
- C. Norotte, F. S. Marga, L. E. Niklason, G. Forgacs, Scaffold-free vascular tissue engineering using bioprinting. *Biomaterials* **30**, 5910–5917 (2009).
- A. M. Blakely, K. L. Manning, A. Tripathi, J. R. Morgan, Bio-pick, place, and perfuse: A new instrument for three-dimensional tissue engineering. *Tissue Eng. Part C Methods* **21**, 737–746 (2015).
- Y. Yu, K. K. Moncal, J. Li, W. Peng, I. Rivero, J. A. Martin, I. T. Ozbolat, Three-dimensional bioprinting using self-assembling scalable scaffold-free “tissue strands” as a new bioink. *Sci. Rep.* **6**, 28714 (2016).
- C.-T. Kuo, C.-L. Chiang, R. Yun-Ju Huang, H. Lee, A. M. Wo, Configurable 2D and 3D spheroid tissue cultures on bioengineered surfaces with acquisition of epithelial–mesenchymal transition characteristics. *NPG Asia Mater.* **4**, e27 (2012).
- E. Fennema, N. Rivron, J. Rouwkema, C. van Blitterswijk, J. de Boer, Spheroid culture as a tool for creating 3D complex tissues. *Trends Biotechnol.* **31**, 108–115 (2013).
- M. Hospodiuk, M. Dey, B. Ayan, D. Sosnoski, K. K. Moncal, Y. Wu, I. T. Ozbolat, Sprouting angiogenesis in engineered pseudo islets. *Biofabrication* **10**, 035003 (2018).
- W. Peng, P. Datta, B. Ayan, V. Ozbolat, D. Sosnoski, I. T. Ozbolat, 3D bioprinting for drug discovery and development in pharmaceuticals. *Acta Biomater.* **57**, 26–46 (2017).
- P. Datta, B. Ayan, I. T. Ozbolat, Bioprinting for vascular and vascularized tissue fabrication. *Acta Biomater.* **51**, 1–20 (2017).
- E. A. Bulanova, E. V. Koudan, J. Degosserie, C. Heymans, F. D. A. S. Pereira, V. A. Parfenov, Y. Sun, Q. Wang, S. A. Akhmedova, I. K. Sviridova, N. S. Sergeeva, G. A. Frank, Y. D. Khesuani, C. E. Pierreux, V. A. Mironov, Bioprinting of a functional vascularized mouse thyroid gland construct. *Biofabrication* **9**, 034105 (2017).
- C. R. Thoma, M. Zimmermann, I. Agarkova, J. M. Kelm, W. Krek, 3D cell culture systems modeling tumor growth determinants in cancer target discovery. *Adv. Drug Deliv. Rev.* **69–70**, 29–41 (2014).
- K. Jakab, C. Norotte, B. Damon, F. Marga, A. Neagu, C. L. Besch-Williford, A. Kachurin, K. H. Church, H. Park, V. Mironov, R. Markwald, G. Vunjak-Novakovic, G. Forgacs, Tissue engineering by self-assembly of cells printed into topologically defined structures. *Tissue Eng. Part A* **14**, 413–421 (2008).
- N. V. Mekhilei, K. S. Lim, G. C. J. Brown, I. Mutreja, B. S. Schon, G. J. Hooper, T. B. F. Woodfield, Automated 3D bioassembly of micro-tissues for biofabrication of hybrid tissue engineered constructs. *Biofabrication* **10**, 024103 (2018).
- L. Gutzweiler, S. Kartmann, K. Troendle, L. Benning, G. Finkenzeller, R. Zengerle, P. Koltay, G. B. Stark, S. Zimmermann, Large scale production and controlled deposition of single HUVEC spheroids for bioprinting applications. *Biofabrication* **9**, 025027 (2017).
- N. I. Moldovan, N. Hibino, K. Nakayama, Principles of the kenzan method for robotic cell spheroid-based three-dimensional bioprinting. *Tissue Eng. Part B Rev.* **23**, 237–244 (2017).
- B. C. Ip, F. Cui, A. Tripathi, J. R. Morgan, The bio-gripper: A fluid-driven micro-manipulator of living tissue constructs for additive bio-manufacturing. *Biofabrication* **8**, 025015 (2016).
- S. H. Ahn, H. J. Lee, J. Puetzer, L. J. Bonassar, G. H. Kim, Fabrication of cell-laden three-dimensional alginate-scaffolds with an aerosol cross-linking process. *J. Mater. Chem.* **22**, 18735–18740 (2012).
- K. Guevorkian, M.-J. Colbert, M. Durth, S. Dufour, F. Brochard-Wyart, Aspiration of biological viscoelastic drops. *Phys. Rev. Lett.* **104**, 218101 (2010).
- Y.-T. L. Dingle, M. E. Boutin, A. M. Chirila, L. L. Livi, N. R. Labriola, L. M. Jakubek, J. R. Morgan, E. M. Darling, J. A. Kauer, D. Hoffman-Kim, Three-dimensional neural spheroid culture: An in vitro model for cortical studies. *Tissue Eng. Part C Methods* **21**, 1274–1283 (2015).
- K. Jakab, B. Damon, F. Marga, O. Doaga, V. Mironov, I. Kosztin, R. Markwald, G. Forgacs, Relating cell and tissue mechanics: Implications and applications. *Dev. Dyn.* **237**, 2438–2449 (2008).
- P. Knüpfer, J. Fritzsche, T. Leistner, M. Rudolph, U. A. Peuker, Investigating the removal of particles from the air/water-interface—Modelling detachment forces using an energetic approach. *Colloids Surf. A Physicochem. Eng. Asp.* **513**, 215–222 (2017).
- A. W. Neumann, R. David, Y. Zuo, *Applied Surface Thermodynamics* (CRC Press, 2010).
- Z. Zhang, J. Xu, B. Hong, X. Chen, The effects of 3D channel geometry on CTC passing pressure—Towards deformability-based cancer cell separation. *Lab Chip* **14**, 2576–2584 (2014).
- V. Heinrich, A. Leung, E. Evans, Nano- to microscale dynamics of P-selectin detachment from leukocyte interfaces. II. Tether flow terminated by P-selectin dissociation from PSGL-1. *Biophys. J.* **88**, 2299–2308 (2005).
- C. Norotte, F. Marga, A. Neagu, I. Kosztin, G. Forgacs, Experimental evaluation of apparent tissue surface tension based on the exact solution of the Laplace equation. *Europhys. Lett.* **81**, 46003 (2008).
- W. Peng, P. Datta, Y. Wu, M. Dey, B. Ayan, A. Dababneh, I. T. Ozbolat, in *Advances in Experimental Medicine and Biology* (Springer, 2018), pp. 53–71.
- R. A. Foty, M. S. Steinberg, The differential adhesion hypothesis: A direct evaluation. *Dev. Biol.* **278**, 255–263 (2005).
- M.-H. Kim, K. Takeuchi, M. Kino-Oka, Role of cell-secreted extracellular matrix formation in aggregate formation and stability of human induced pluripotent stem cells in suspension culture. *J. Biosci. Bioeng.* **127**, 372–380 (2019).
- F. Bresme, M. Oettel, Nanoparticles at fluid interfaces. *J. Phys. Condens. Matter* **19**, 413101 (2007).
- A. Kumar, B. J. Park, F. Tu, D. Lee, Amphiphilic janus particles at fluid interfaces. *Soft Matter* **9**, 6604–6617 (2013).
- P. Del Gaudio, P. Colombo, G. Colombo, P. Russo, F. Sonvico, Mechanisms of formation and disintegration of alginate beads obtained by prilling. *Int. J. Pharm.* **302**, 1–9 (2005).
- D. Szabó, S. Akiyoshi, T. Matsunaga, J. P. Gong, Y. Osada, M. Zrinyi, Spreading of liquids on gel surfaces. *J. Chem. Phys.* **113**, 8253–8259 (2000).
- H. Gudapati, M. Dey, I. Ozbolat, A comprehensive review on droplet-based bioprinting: Past, present and future. *Biomaterials* **102**, 20–42 (2016).
- T. Bhattacharjee, S. M. Zehnder, K. G. Rowe, S. Jain, R. M. Nixon, W. G. Sawyer, T. E. Angelini, Writing in the granular gel medium. *Sci. Adv.* **1**, e1500655 (2015).
- Y. Wu, M. Hospodiuk, W. Peng, H. Gudapati, T. Neuberger, S. Koduru, D. J. Ravnic, I. T. Ozbolat, Porous tissue strands: Avascular building blocks for scalable tissue fabrication. *Biofabrication* **11**, 015009 (2019).
- J. R. Gallant, L. L. Traeger, J. D. Volkening, H. Moffett, P.-H. Chen, C. D. Novina, G. N. Phillips Jr., R. Anand, G. B. Wells, M. Pinch, R. Güth, G. A. Unguez, J. S. Albert, H. H. Zakon, M. P. Samanta, M. R. Sussman, Genomic basis for the convergent evolution of electric organs. *Science* **344**, 1522–1525 (2014).
- E. Laliberté, G. Zemunik, B. L. Turner, Environmental filtering explains variation in plant diversity along resource gradients. *Science* **345**, 1602–1605 (2014).
- M. S. Mannoor, Z. Jiang, T. James, Y. L. Kong, K. A. Malatesta, W. O. Soboyejo, N. Verma, D. H. Gracias, M. C. McAlpine, 3D printed bionic ears. *Nano Lett.* **13**, 2634–2639 (2013).
- K. T. Morin, R. T. Tranquillo, In vitro models of angiogenesis and vasculogenesis in fibrin gel. *Exp. Cell Res.* **319**, 2409–2417 (2013).
- E. Zudaire, L. Gambardella, C. Kurcz, S. Vermeren, A computational tool for quantitative analysis of vascular networks. *PLOS ONE* **6**, e27385 (2011).
- D. J. Gould, T. J. Vadakkan, R. A. Poché, M. E. Dickinson, Multifractal and lacunarity analysis of microvascular morphology and remodeling. *Microcirculation* **18**, 136–151 (2011).
- L. N. Handly, A. Pilko, R. Wollman, Paracrine communication maximizes cellular response fidelity in wound signaling. *ELife* **4**, e09652 (2015).
- D. Guidolin, P. Rebuffat, G. Albertin, Cell-oriented modeling of angiogenesis. *ScientificWorldJournal* **11**, 1735–1748 (2011).
- D. Fukumura, R. Xavier, T. Sugiyama, Y. Chen, E. C. Park, N. Lu, M. Selig, G. Nielsen, T. Taksir, R. K. Jain, B. Seed, Tumor induction of VEGF promoter activity in stromal cells. *Cell* **94**, 715–725 (1998).
- A. C. Newman, M. N. Nakatsu, W. Chou, P. D. Gershon, C. C. W. Hughes, The requirement for fibroblasts in angiogenesis: Fibroblast-derived matrix proteins are essential for endothelial cell lumen formation. *Mol. Biol. Cell* **22**, 3791–3800 (2011).
- W. G. Chang, J. W. Andrejcsk, M. S. Kluger, W. M. Saltzman, J. S. Pober, Pericytes modulate endothelial sprouting. *Cardiovasc. Res.* **100**, 492–500 (2013).
- C. Galustian, J. Dye, L. Leach, P. Clark, J. A. Firth, Actin cytoskeletal isoforms in human endothelial cells in vitro: Alteration with cell passage. *In Vitro Cell. Dev. Biol. Anim.* **31**, 796–802 (1995).
- T. Menge, M. Gerber, K. Wataha, W. Reid, S. Guha, C. S. Cox Jr., P. Dash, M. S. Reitz Jr., A. Y. Khakoo, S. Pati, Human mesenchymal stem cells inhibit endothelial proliferation and angiogenesis via cell–cell contact through modulation of the VE-cadherin/β-catenin signaling pathway. *Stem Cells Dev.* **22**, 148–157 (2013).
- K. Otsu, S. Das, S. D. Houser, S. K. Quadri, S. B. Bhattacharya, Concentration-dependent inhibition of angiogenesis by mesenchymal stem cells. *Blood* **113**, 4197–4205 (2009).
- M. F. Pittenger, A. M. Mackay, S. C. Beck, R. K. Jaiswal, R. Douglas, J. D. Mosca, M. A. Moorman, D. W. Simonetti, S. Craig, D. R. Marshak, Multilineage potential of adult human mesenchymal stem cells. *Science* **284**, 143–147 (1999).
- Y. Wu, H. Cao, Y. Yang, Y. Zhou, Y. Gu, X. Zhao, Y. Zhang, Z. Zhao, L. Zhang, J. Yin, Effects of vascular endothelial cells on osteogenic differentiation of noncontact co-cultured periodontal ligament stem cells under hypoxia. *J. Periodontol. Res.* **48**, 52–65 (2013).

53. M. Westhrin, M. Xie, M. Ø. Olderøy, P. Sikorski, B. L. Strand, T. Standal, Osteogenic differentiation of human mesenchymal stem cells in mineralized alginate matrices. *PLOS ONE* **10**, e0120374 (2015).
54. N. Rajan, J. Habermehl, M.-F. Coté, C. J. Doillon, D. Mantovani, Preparation of ready-to-use, storable and reconstituted type I collagen from rat tail tendon for tissue engineering applications. *Nat. Protoc.* **1**, 2753–2758 (2006).
55. J. W. Nichol, S. T. Koshy, H. Bae, C. M. Hwang, S. Yamanlar, A. Khademhosseini, Cell-laden microengineered gelatin methacrylate hydrogels. *Biomaterials* **31**, 5536–5544 (2010).

Acknowledgments: We thank J. Gallant from Michigan State University for providing electric fish and B. Cheng from PSU for providing a high-speed camera for contact angle measurements. We thank Y. Wu, D. Sosnoski, D. N. Branford, and M. A. Alioglu from PSU for assistance in providing tissue strands, culturing cells, designing the graphics for Fig. 1, and maintaining electric fish, respectively. We are also grateful to D. Ravnic and S. Koduru (Department of Surgery at PSU) for providing ADSCs, N. Zavazava (Department of Internal Medicine at the University of Iowa) for providing HDFs, and A. Mastro (Department of Biochemistry and Molecular Biology at PSU) for providing 3T3 and 4T1 cells. We thank RoosterBio for providing MSCs and GM. We also acknowledge the support from The Huck Institutes of Life Sciences and Materials Research Institute for providing facilities for

characterization of experiments. **Funding:** This work has been supported by NSF awards 1914885 (I.T.O.) and 1624515 (I.T.O.), NIH award R21 CA224422 01A1 (I.T.O.), and a Convergence grant from the Materials Research Institute at PSU (I.T.O.). B.A. acknowledges the support from the Turkish Ministry of National Education. **Author contributions:** B.A., D.N.H., M.D., and I.T.O. designed the research. B.A., Z.Z., C.D., and I.T.O. completed the theoretical work. B.A., D.N.H., Z.Z., M.D., and A.P. performed the experiments. All authors contributed to writing the manuscript and agreed on the final content of the manuscript. **Competing interests:** The authors declare that they have no competing interests. **Data and materials availability:** All data needed to evaluate the conclusions in the paper are present in the paper and/or the Supplementary Materials. Additional data related to this paper may be requested from the authors.

Submitted 31 January 2019

Accepted 13 December 2019

Published 6 March 2020

10.1126/sciadv.aaw5111

Citation: B. Ayan, D. N. Heo, Z. Zhang, M. Dey, A. Povilianskas, C. Drapaca, I. T. Ozbolat, Aspiration-assisted bioprinting for precise positioning of biologics. *Sci. Adv.* **6**, eaaw5111 (2020).

Aspiration-assisted bioprinting for precise positioning of biologics

Bugra Ayan, Dong Nyoung Heo, Zhifeng Zhang, Madhuri Dey, Adomas Povilianskas, Corina Drapaca and Ibrahim T. Ozbolat

Sci Adv **6** (10), eaaw5111.
DOI: 10.1126/sciadv.aaw5111

ARTICLE TOOLS

<http://advances.sciencemag.org/content/6/10/eaaw5111>

SUPPLEMENTARY MATERIALS

<http://advances.sciencemag.org/content/suppl/2020/03/02/6.10.eaaw5111.DC1>

REFERENCES

This article cites 53 articles, 6 of which you can access for free
<http://advances.sciencemag.org/content/6/10/eaaw5111#BIBL>

PERMISSIONS

<http://www.sciencemag.org/help/reprints-and-permissions>

Use of this article is subject to the [Terms of Service](#)

Science Advances (ISSN 2375-2548) is published by the American Association for the Advancement of Science, 1200 New York Avenue NW, Washington, DC 20005. The title *Science Advances* is a registered trademark of AAAS.

Copyright © 2020 The Authors, some rights reserved; exclusive licensee American Association for the Advancement of Science. No claim to original U.S. Government Works. Distributed under a Creative Commons Attribution NonCommercial License 4.0 (CC BY-NC).